Poly(d,l -lactide)-Grafted Bioactive Glass Nanoparticles: From Nanobricks to Freeze-Cast Scaffolds for Bone Substitution

Prescillia Lagarrigue, Vincent Darcos, Christophe Tenailleau, Benjamin Duployer, Agnès Dupret-Bories, Sophie Cazalbou, Dominique Poquillon, David Grossin, Christèle Combes, Jérémy Soulié

Poly(D,L-lactide)-Grafted Bioactive Glass Nanoparticles : from Nano-Bricks to Freeze-Cast Scaffolds for Bone Substitution

P. Lagarrigue*[a,b], V. Darcos,[b] C. Tenailleau,[c] B. Duployer,[c] A. Dupret-Bories,[a,d] S. Cazalbou,[c] D. Poquillon,[a] D. Grossin,[a] C. Combes,[a] and J. Soulié*[a]

[a]CIRIMAT, Université de Toulouse, CNRS, Toulouse INP - ENSIACET, 4 allée Emile Monso - BP44362, 31030 Toulouse, France

[b]IBMM, Univ Montpellier, CNRS, ENSCM, Montpellier, France

[c]CIRIMAT, Université de Toulouse, CNRS, Université Toulouse 3 - Paul Sabatier, 118 Route de Narbonne, 31062 Toulouse, France

[d]Chirurgie ORL et Cervico-faciale, IUCT Toulouse Oncopole, Institut Claudius-Regaud, Toulouse, France

*Corresponding authors: Prescillia Lagarrigue (prescillia.lagarrigue@toulouse-inp.fr), Jérémy Soulié (jeremy.soulie@ensiacet.fr).

ABSTRACT

This paper focuses on a new integrative “bricks-and-mortar" approach involving bioactive glass nanoparticles (bricks) covalently functionalized with a customized polymer (mortar) combined with the freeze-casting process. With the aim to obtain a macroporous composite for bone substitution, constituted of a spatially homogeneous assembly of nanoscale objects, we established a method for the systematic elaboration of nanocomposite scaffolds. It was implemented through several steps, from the synthesis of functionalized poly(D,L-lactide) (PDLLA) and SiO_2-CaO binary bioactive glass nanoparticles (diameter around 164 nm) to the unidirectional freeze-casting process. The different stages include the first description of controlled PDLLA (M_n 8400 g.mol^{-1}) grafting onto bioactive glass nanoparticles surface, their fine characterization and grafting quantification, and their mixing with free PDLLA chains (83 400 g.mol^{-1}) during suspension formulation. This article emphasized the effect of the working temperature during the freeze-casting process on the multiscale spatial organization of resulting scaffolds such as the porosity morphology (lamellar and tubular), size (from 30 to 380 μm), anisotropy and orientation. Beyond porosity, our results demonstrate a rosaries-like organization of PDLLA-grafted nanoparticles in pore walls. The higher homogeneity in spatial distribution of grafted nanoparticles over the height of scaffolds and at a micron-scale, confirms the validity of the “bricks-and-mortar” concept to prevent or limit aggregation. In particular, this study highlights the correlation between nanoparticle functionalization and mechanical properties, especially the recovery rate after compression tests. These results lay the foundation for the development of tunable materials for bone substitution, *via* potential enhancement of bioactivity and cell colonization.

KEYWORDS

Bricks and mortar; bioactive glass; poly(D,L-lactide); scaffolds; nanocomposite; freeze-casting; bone substitution

1. INTRODUCTION

Small bone defects related or consecutive to maxillofacial pathologies/surgeries require medical implants of a few cubic centimeters for bone reconstruction. Such kind of biomaterial should [1,2]: i) stimulate the formation of new bone in critical bone defects thanks to cell differentiation and proliferation; ii) be osteoconductive and promote cell adhesion; iii) exhibit high porosity (pore size, anisotropy, volume) in order to support cell colonization and angiogenesis; iv) maintain adequate mechanical properties during manipulation by the surgeon; v) be resorbed after at least 6 months; vi) demonstrate additional properties such as pro-angiogenic and antibacterial effects for some pathologies like mandibular osteoradionecrosis.

Among inorganic materials for bone substitution, silicate-based bioactive glasses (or “bioglasses”) [3] meet the first two criteria previously listed. Indeed, when implanted, their dissolution allows the release of silicic acid $Si(OH)_4$ that stimulates collagen I formation and osteoblastic differentiation [4]. Their bioactivity is also related to the formation of a biomimetic apatite layer on their surface after implantation by incorporating Ca^{2+} and PO_4^{3-} ions released from bioglass, thus favoring the adhesion and proliferation of osteoblasts [5]. Beyond their involvement in apatite precipitation to mineralize extracellular matrix, these free ions also enhance osteoblast proliferation, differentiation and increase expression of growth factors (IGF-I or IGF-II) and the matrix Gla protein (MGP), a key regulator in bone formation [6]. Integration of doping ions (Cu^{2+}, Ag^{+}, Sr^{2+}) in the glassy network could enhance osteogenesis, prevent the resistance to antibiotics and favor vascularization [7]. Although both sol-gel and melt-derived bioactive glasses have demonstrated excellent biological properties, their brittle nature prevents them to be used be used as bulk materials in applications requiring cyclic loads and is prohibitive for their cut by surgeons [8,9].

These drawbacks can be avoided coupling them with polymers to develop composites materials. Bioglasses can be associated to natural [10,11] or synthetic [12,13] polymer matrices. Among the latter, aliphatic polyesters such as poly(lactide) (PLA) or poly(ε-caprolactone) have a special place due to their well-known biodegradability and biocompatibility [14]. Their mixture with bioglass particles improves scaffolds mechanical properties (mineral fillers minimize the chains mobility, increasing rigidity) and decreases the autocatalytic acidic polymer degradation by playing a buffering role and limiting acidification [15]. Beyond composition and considering defects induced by maxillofacial pathologies and especially mandibular

surgeries, adequate biomaterials should mimic mandibular trabecular bone with an open porosity (70-80 % vol.) favoring fluid and cells percolation and pore sizes of 150-400 µm with partial anisotropic orientation of porosity/trabecules [16]. Although various interesting processes such as electrospinning [17], hard template methods [18], 3D-printing [19] or supercritical CO_2 [20–22] were reported, very few direct comparisons between respective advantages have been described.

In this contribution, the freeze-casting process has been chosen for its robustness, reproducibility and the control of pore size and anisotropy [23]. It is based on solvent crystals nucleation and growth until total solidification and its subsequent sublimation. The overall process allows to control porosity size (small or hierarchical porosity can be reached), anisotropy and volume. This process has already been used for porous aliphatic polyesters/bioactive glass composites [24–27]. However, the described methodology based on a simple mixture of melt-derived glass particles of several dozen microns with polymers, generally leads to a poor dispersion of the charges in the polymer matrix (aggregation) and therefore to spatial inhomogeneity of the properties (especially due to the effect of gravity during the process). It may result in the degradation of preferential zones and mechanical weakening of some pore walls. The degradation can be made more congruent by elaborating composites in which organic and inorganic parts are intimately mixed [8]. For this purpose, Jones [28,29] and then Lao [9,30] developed hybrid scaffolds in which silicate and polymeric network are covalently linked. Despite the success of this synthesis route, the co-integration of major (Ca^{2+}) and/or doping (Cu^{2+}, Sr^{2+}, Ag^{+}) bivalent/monovalent ions in the silicate network remains a challenge as no high thermal treatment can be carried out on these materials.

The present paper aspires to propose as alternative to hybrid scaffolds, *via* an original and integrative “bricks-and-mortar" approach involving bioactive glass nanoparticles (bricks in which bivalent ions can be inserted thanks to temperature) covalently functionalized with customized polymer (mortar) combined with the freeze-casting process. Slightly different definitions of the "bricks-and-mortar" strategy can be used depending on the scientific community [31]. Considering the one detailed by Stucky *et al.* [32], this concept leads to a controlled assembly of nanoscale objects into composite materials *via* suitable and more or less complex or specific function/layer (as a polymer) on their surface that acts as a “linker” between particles. This approach is bio-inspired by bone (apatite-collagen) and nacre (aragonite-chitin) [33]. This concept has been used for some compounds (TiO_2-Chitosan, SiO_2-PVA) [34] but, to the best of our knowledge, never for bioactive glass nanocomposites in the biomedical field.

In this study, we established a method for the step-by-step fabrication of nanocomposite scaffolds, from the synthesis of functionalized poly(D,L-lactide) (PDLLA) and SiO_2-CaO binary glasses system bioglass nanoparticles to the unidirectional freeze-casting process the latter nanosystems. Intermediate steps include an unprecedented description of controlled grafting of PDLLA onto the surface of binary nanoparticles, their fine characterization (TEM, SEM-FEG, DLS, NMR, ICP-OES, FTIR, TGA, specific surface area measurements) and grafting quantification and their mixing with free polymer chains during suspension formulation (Figure 1). Beyond the synthesis of such composite nanosystems, this experimental work focuses on the effect of both the freezing temperature applied to the nanocomposite suspension and the nanoparticle functionalization on the multiscale spatial organization of resulting scaffolds (FEG-SEM, Hg intrusion, microtomography) and their mechanical behavior (uniaxial compression tests).

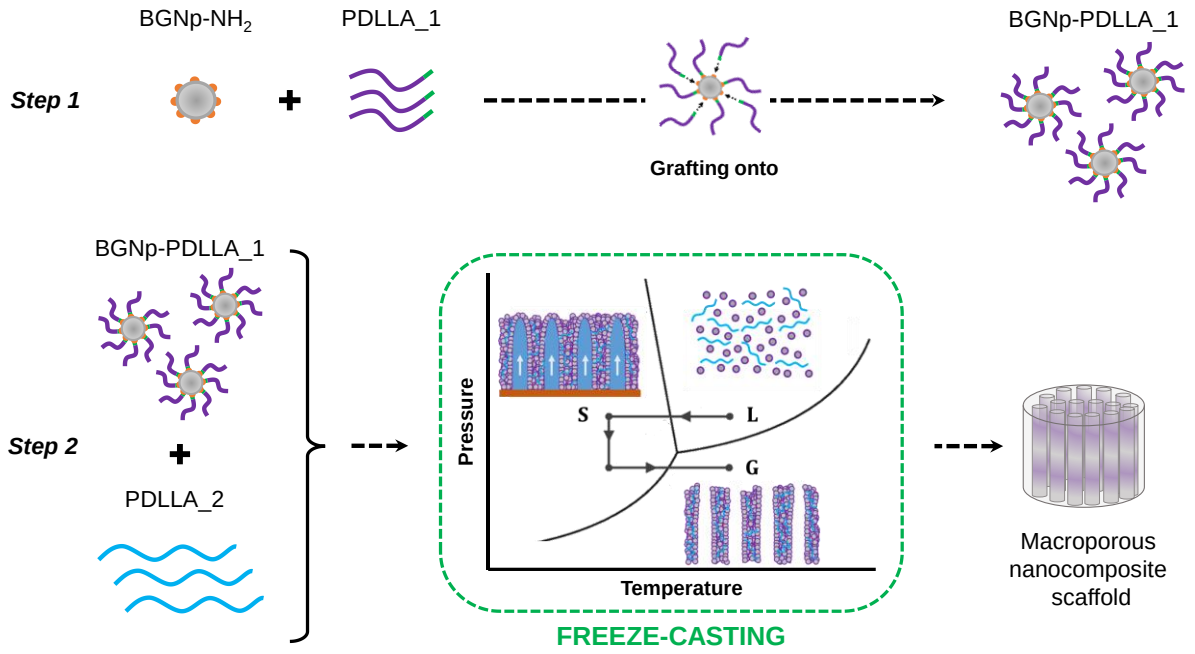

Figure 1. Scheme of the strategy followed for nanocomposite scaffolds elaboration. Herein, BGNp-NH_2 are the amino-functionalized bioglass nanoparticles, PDLLA_1 is N-hydroxysuccinimide ester poly(D,L-lactide), BGNp-PDLLA_1 are PDLLA-grafted bioglass nanoparticles and PDLLA_2 are high molecular weight free chains of poly(D,L-lactide).

2. EXPERIMENTAL SECTION

2.1. Materials

D,L-lactide was purchased from Corbion Purac (PURASORB® DL Goerinchem). Stannous 2-ethyl hexanoate ($Sn(Oct)_2$), 4-(dimethylamine)pyridine (DMAP), succinic anhydride (SA), *N*,*N*′-dicyclohexyl carbodiimide (DCC), tetraethyl orthosilicate (TEOS), calcium nitrate tetrahydrate ($Ca(NO_3)_2$, 4 H_2O), 3-aminopropyl triethoxysilane (APTES), ammonium hydroxide solution (28–30% NH_3 basis), absolute ethanol, 1,4-dioxane, dimethyl carbonate (DMC) and ethyl acetate were purchased from Sigma-Aldrich and used without any further purification. *N*-hydroxysuccinimide (NHS) was purchased from ACROS. Benzyl alcohol (BnOH), triethylamine (TEA), dichloromethane, toluene and *N*,*N*-dimethylformamide (DMF) were purchased from Sigma-Aldrich. BnOH and TEA were dried over potassium hydroxide for 24 hours while dichloromethane, toluene and DMF were dried over calcium hydride before distillation. Ultrapure water with resistivity of 18 MΩ.cm was produced thanks to a Millipore Milli-Q water system.

2.2. Synthesis of poly(D,L-lactide)-grafted bioglass nanoparticles (BGNp-PDLLA_1)

2.2.1. Synthesis of N-hydroxysuccinimide ester poly(D,L-lactide) (PDLLA_1)

The synthesis of *N*-hydroxysuccinimide ester poly(D,L-lactide) (PDLLA–COO–NHS) was performed as described in a previous paper [35], using as starting polymer a poly(D,L-lactide), ***PDLLA-OH***, with a theoretical molecular weight of $M_{n,th}$ 10 200 g.mol^{-1} (feed ratio for ring-opening polymerization [D,L-lactide]$_0$/[BnOH]$_0$/[$Sn(Oct)_2$]$_0$ set at 70/1/0.1). Thus, obtained polymer chains, named herein ***PDLLA_1***, were used during the synthesis of PDLLA-grafted bioglass nanoparticles as described below.

^{1}H NMR (300 MHz, $CDCl_3$, δ (ppm)): 7.3 (m, C_6H_5); 5.11 (m, C*H*-CH_3); 2.98 (d, COO-CH_2-CH_2-COO); 2.83 (m, COO-CH_2-CH_2-COO + CO-CH_2-CH_2-CO); 1.52 (d, CH-CH_3), $M_{n,\ NMR}$ = 8 400 g.mol^{-1}, $M_{n,SEC}$ = 14 200 g.mol^{-1}, Đ = 1.52

2.2.2. Synthesis of poly(D,L-lactide) in bulk (PDLLA_2)

High molecular weight PDLLA was synthesized in bulk by ring-opening polymerization of D,L-lactide. Typically, to obtain PDLLA with a theoretical molecular weight of $M_{n,th}$ 50 000 g.mol^{-1}, 100 g of D,L-lactide

(0.69 mol), 80 mg of $Sn(Oct)_2$ (0.20 mmol) and 214 mg of BnOH (2.0 mmol) were introduced into a sealed flask. The flask was degassed by ten vacuum-argon cycles and sealed. The synthesis was then performed in a polymerization oven at 130 °C during 2 days under constant stirring. The obtained mixture was then dissolved in dichloromethane and poured into cold ethanol. The precipitated polymer was collected by filtration and dried under vacuum. The resulting polymer, named ***PDLLA_2***, was used as free polymer chains during the nanocomposite scaffolds elaboration to enhance links formation between PDLLA-grafted bioglass nanoparticles.

^{1}H NMR (300 MHz, $CDCl_3$, δ (ppm)): 7.3 (m, C_6H_5); 5.11 (m, C*H*-CH_3); 4.33 (q, (CH_3)C*H*-OH); 1.52 (m, CH-CH_3), $M_{n,SEC}$ = 83 400 g.mol^{-1}, $Đ$ = 1.83.

2.2.3. Synthesis of bioglass nanoparticles

Bioglass nanoparticles (***BGNp***) with a binary composition (SiO_2-CaO, nominal molar ratio Si:Ca of 85:15) were synthesized following a modified Stöber process based on Greasley *et al.* procedure [36]. Firstly, to synthesize silica nanoparticles, 1.3 L of ethanol, MiliQ water (6 M) and ammonium hydroxide (0.28 M) were mixed under vigorous stirring. After 30 minutes, TEOS (0.28 M), pre-mixed with 200 mL of ethanol, was added one shot into the solution and the latter was left under stirring during 17 hours. Resulting silica nanoparticles were collected by centrifugation (10 min at 4 200 rpm) and redispersed into 100 mL of MiliQ water using ultrasonic probe (15 min). Then, 0.642 M of calcium nitrate tetrahydrate was added to the suspension under stirring. After 45 minutes, the suspension was centrifuged (15 min at 4 200 rpm) and the collected pellet was frozen and freeze-dried for 3 days (-80 °C, 0.120 mbar). Finally, the particles were heated under airflow at 680 °C (heating rate of 3 °C/min with a 3 hours dwell at 680 °C) in order to remove nitrate and ensure calcium incorporation into the silica network.

2.2.4. Synthesis of PDLLA-grafted bioglass nanoparticles (BGNp-PDLLA_1)

PDLLA-grafted bioglass nanoparticles (***BGNp-PDLLA_1***) were synthesized by adapting a grafting protocol described in a previous work [35]. Briefly, amino-functionalized bioglass nanoparticles were obtained by reaction with 3-aminopropyl triethoxysilane (APTES) in anhydrous toluene under inert atmosphere. Then amino-functionalized nanoparticles were grafted with ***PDLLA_1*** using "grafting onto" method in DMF and in presence of triethylamine. The resulting ***BGNp-PDLLA_1*** were washed twice with toluene and twice with ethyl acetate (dispersion/centrifugation) to remove remaining PDLLA free chains. Finally, nanoparticles were dried under vacuum during 2 days. The obtained PDLLA-grafted bioglass nanoparticles, considered as "bricks" according to "bricks-and-mortar" approach, were used as building blocks during nanocomposite scaffolds elaboration by freeze-casting.

2.3. Elaboration of macroporous nanocomposite scaffolds by freeze-casting

2.3.1. Preparation of nanocomposite suspension

The nanocomposite suspension was prepared using dimethyl carbonate (DMC) as solvent. The latter, apart from being a PDLLA solvent, is a no cytotoxic solvent and possesses a solidification temperature easily reachable (T_f = 2-4 °C). The nanocomposite suspension with a [***PDLLA_2***]/[***BGNp-PDLLA_1***] weight % ratio of 51/49 and a [***PDLLA_2***] concentration of 2.5 w/v % in DMC was prepared following two steps. Firstly, the corresponding amount of ***BGNp-PDLLA_1*** was dispersed in DMC and the suspension homogenized using an ultrasonic probe during 10 minutes. Then, ***PDLLA_2*** was added to the suspension and the latter was mixed using a vortex until total ***PDLLA_2*** dissolution (3-5 min). The nanocomposite suspensions were prepared just before mold casting and unidirectional freeze-casting process.

2.3.2. Unidirectional freeze-casting

In this study, 4.6 mL of suspension were poured in transparent cylindrical fluorinated ethylene propylene molds (inner diameter: 2.1 cm), closed with copper caps. The filled molds were then placed on copper cold fingers, part of homemade freeze-casting devices. The temperature of the latter was chosen below solvent solidification temperature, either at -10 °C or at -160 °C in order to study the impact of the working temperature (T_W) on the final multiscale organization and scaffolds properties. During these experiments (5 hours for T_W -10 °C, 15 min for T_W -160 °C), the molds were thermally insulated with

polyurethane homemade foams to ensure unidirectional solidification front, and thus unidirectional DMC crystals growth, all along the sample. A representative scheme of the used device is presented in Supporting Information (Figure S1). After total solidification of the suspension, molds were opened and solidified suspension were freeze-dried for 12 hours (-80 °C, 0.120 mbar), allowing solvent sublimation. The obtained scaffolds are named **S10** and **S160** for the ones elaborated at -10 °C and -160 °C, respectively. For comparison, a suspension containing non-grafted bioglass nanoparticles (***BGNp***) and free polymer (***PDLLA_2***) was prepared and freeze-cast in the same conditions. Resulting scaffolds were labelled $\mathbf{S_{NG}10}$.

2.4. Characterization methods

2.4.1. Polymer characterization

The synthesized and functionalized PDLLAs were characterized by ^{1}H NMR and size exclusion chromatography (SEC). ^{1}H NMR spectra were recorded using a Bruker spectrometer (AMX300) operating at 300 MHz in $CDCl_3$ as solvent. The chemical shifts were referenced to the peak of residual non-deuterated solvents. SEC was operated to evaluate average molecular weights (M_n) and dispersities ($Đ$). Analyses were performed on a Shimadzu Prominence system (Shimadzu Corp, Kyoto, Japan), equipped with a PLgel MIXED-C guard column (Agilent, 5 µm, 50 × 7.5 mm), two mixed medium columns PLgel MIXED-C (5 µm, 300 × 7.8 mm) and a Shimadzu RI detector 20-A. THF was used as mobile phase with a flow of 1 mL.min^{-1} at 35 °C. Polystyrene standards were used for calibration and polymers characteristics obtained expressed according to those standards.

2.4.2. PDLLA-grafted bioglass nanoparticles characterization

Initial bioglass nanoparticles (***BGNp***) and PDLLA-grafted bioglass nanoparticles (***BGNp-PDLLA_1***) morphology were analyzed using transmission electron microscopy (TEM). Samples were prepared by dispersing nanoparticles in absolute ethanol (0.5 mg.mL^{-1}) and deposited on 300 mesh copper TEM grids. Imaging was performed on JEOL JEM 1400 using an operating voltage of 120 kV. Multiple areas of each grid were analyzed and, for nanoparticle size determination, at least 100 particles were measured to calculate mean particle diameter (D_{av}) and standard deviation by image processing (ImageJ, with "Analyze particles" tool). Complementary characterizations (DLS, Zeta potential, specific surface area, ^{29}Si SS NMR) of ***BGNp*** and ***BGNp-PDLLA_1*** are presented in supporting information.

Cross polarization magic angle spinning ^{29}Si solid state nuclear magnetic resonance spectroscopy analysis (CP-MAS ^{29}Si NMR spectroscopy) was performed to characterize the modification of the silica network due to the calcium incorporation. Analyses were performed on a Bruker Avance III HD 400 spectrometer (9.4 T) and 4 mm zirconia rotors. Samples were analyzed over 10 cross polarization periods of 1.1 ms separated by a ^{1}H repolarization time of 0.9 s and with a recycle time of 3 s [37]. Chemical shifts are relative to TMS.

Fourier transformed infrared (FTIR) spectroscopy analyses were performed on ***PDLLA_1***, ***BGNp*** and ***BGNp-PDLLA_1*** in KBr pellet in transmission mode using a Nicolet 5700 spectrometer (400-4000 cm^{-1}, 64 scans, resolution 4 cm^{-1}). We prepared pellets by mixing 1 mg of nanoparticles or polymer with 300 mg of KBr then pressed at 8 tons.

Bioglass nanoparticles composition (concentration of calcium and silicon) was determined using inductively coupled plasma optical emission spectroscopy (ICP-OES, Horiba Jobin Yvon Ultima2, Japan). Samples were prepared using the quantitative method of alkaline fusion paired with acidic digestion as described previously [38].

2.4.3. Macroporous nanocomposites characterization

Scanning electron microscopy (SEM) was used to investigate scaffolds porous structure (anisotropy, porosity dimensions, wall aspect and thickness). Images were acquired on FEI Quanta 450 SEM both in secondary and backscattered electron mode and porous structure was analyzed using image processing (Image J). Field emission gun-scanning electron microscopy (FEG-SEM JEOL JSM-7800F Prime) was also performed on scaffolds samples. Platinum was sputtered on scaffolds surface before imaging to limit electron accumulation.

X-ray computed microtomography images were performed to evaluate the three-dimensional morphology and multiscale organization of the scaffolds. A Phoenix/GE Nanotom 180 instrument using a tungsten target (mode 0) was used at a voltage of 60 kV and a current of 260 µA. Samples were positioned at 70 mm from RX target and at 280 mm from detector. With counting time of 750 ms per picture and an average of five pictures per 0.25° step. Datos X software was used to process the data and reconstruct 3D images of the scaffolds. Images were treated using the Vg Studio Max software. The maximum voxel size was 10 µm with a magnification of 5.

Pore sizes and surface percent porosity were determined by image processing using *ImageJ* software. Concerning porosity size, the porosity range and pores sizes were evaluated on more than 30 pores and the size histogram were adjusted with a log-normal distribution.

The porosity of scaffolds was also studied using a mercury intrusion porosimeter (AutoPore III, Micromeritics Instruments Inc., Norcross, GA), which allows detection of pores in the range 360–0.003 µm. The total percentage porosity was calculated by: $P_{tot} = d_{app} \times V_{Hg} \times 100$ where d_{app} is the apparent density of the scaffold and V_{Hg} is the total mercury intrusion volume per gram of specimen analyzed. The pore size distribution was calculated as the differential mercury intrusion volume plotted versus the pore size.

Uniaxial compressive tests were performed on the cylindrical scaffolds (height ≈ 1.1 cm, diameter ≈ 2.1 cm) using a MTS Criterion Model 42 electromechanical test systems equipped with a 2 kN load cell. All tests were controlled by imposing the displacement of the upper plate used to axially compress the samples. The displacement rate during loading and unloading was 0.085 mm/s. Since the flatness of the top surface of the specimens could have imperfections, due to molding, an initial preload up to a compression of 2 N has been applied to improve the flatness of the contact surface before testing. The tests were performed until the compression load reached -20 N, corresponding to the mean force applied by surgeons on materials during implantation (measured with a load cell by surgeon). The data acquisition frequency was 1 Hz. The tests were performed on 3 samples for each kind of scaffolds. The height of the cylinder was measured at the end of the test, after unloading the specimen, and then 24 hours after to estimate scaffolds recovery. It allows estimating the viscoelastic deformation, making the hypothesis that residual deformation after 24 hours is linked to irreversible processes (plastic deformation, damages...).

3. RESULTS AND DISCUSSION

3.1. Synthesis of PDLLA-grafted bioglass nanoparticles

3.1.1. Polymer synthesis

Two different kind of polymers were synthesized. *N*-hydroxysuccinimide ester poly(D,L-lactide) (PDLLA-COO-NHS, ***PDLLA_1***), used for PDLLA-grafted BGNp synthesis, was obtained by post-polymerization modification of poly(D,L-lactide) following a protocol (Scheme S1) already described in a previous work [35]. High molecular weight poly(D,L-lactide), ***PDLLA_2***, added to the nanocomposite suspension before freeze-casting process, was prepared by ring-opening polymerization (ROP) in bulk.

Concerning ***PDLLA_1*** synthesis, starting polymer, ***PDLLA-OH***, with a theoretical molecular weight of M_n 10200 g.mol^{-1} was prepared by ROP of D,L-lactide in solution using a feed ratio D,L-lactide/benzyl alcohol/Sn(Oct)$_2$ of 70/1/0.1. The obtained ***PDLLA-OH*** was characterized both by ^{1}H NMR spectroscopy (Figure S2 - A) and SEC analysis in THF with PS standards (Figure S2-B). The ***PDLLA-OH*** molecular weight, $M_{n,\,NMR}$ 8 400 g.mol^{-1}, was determined using the relative intensity of NMR signals of lactic acid units (δ 5.11 ppm, b and δ 4.33 ppm, d) and phenyl group (δ 7.3 ppm, a) [35]. Molecular weight evaluated using SEC analysis in THF with PS standards (Figure S2-B), $M_{n,\,SEC}$ 14 200 g.mol^{-1}, is higher than the one determined by ^{1}H NMR. Indeed, the overestimation of the molecular weight for aliphatic polyesters such as polylactides using SEC with PS standards is well-known [39,40]. The slightly high dispersity value, $Đ$ 1.52, can be explained by the presence of transesterification reaction during the ***PDLLA-OH*** synthesis. The *N*-hydroxysuccinimide ester poly(D,L-lactide) (PDLLA-COO-NHS, ***PDLLA_1***) was then synthesized by conjugative chemistry using a two steps process (Scheme S1). The ^{1}H NMR spectrum of the obtained ***PDLLA_1*** (PDLLA-COO-NHS) is presented in Figure S2-A. The results confirm the quantitative functionalization of ***PDLLA-OH*** in PDLLA-COO-NHS thanks to the presence of a triplet and a multiplet respectively at δ 2.98 ppm and δ 2.83 ppm related to two hydrogen atoms from SA (e) and overlap of two

hydrogen atoms from SA (e') and hydrogen atoms from terminal NHS moiety (f). The functionalization rate (96 %) was determined comparing the relative peak area of SA and NHS protons overlap at δ 2.83 ppm (f + e') with the PDLLA backbone multiplet at δ 5.11 ppm (b, d). These results corroborate that the two-step process based on ***PDLLA-OH*** customization with SA and NHS/DCC developed previously [35] can be applied to higher molecular weight ***PDLLA-OH*** with high functionalization rate.

A high molecular weight poly(D,L-lactide) ($M_{n,\,th}$ 50 000 g.mol^{-1}), named ***PDLLA_2***, was also synthesized by ROP of D,L-lactide in bulk. This polymer was used in the further step to improve nanocomposite scaffolds cohesion and properties. The synthesis was performed using $Sn(Oct)_2$ as catalyst and benzyl alcohol as initiator with a feed ratio D,L-lactide/initiator of 350/1. The conversion of D,L-lactide was quantitative and the molecular weight of the resulting polymer was characterized using SEC analysis in THF with PS standards. The Figure 3 presents the ***PDLLA_2*** SEC trace, corresponding to a molecular weight of $M_{n,\,SEC}$ 83 400 g.mol^{-1} and a dispersity of $Đ$ 1.83. As discussed earlier, SEC analysis give higher molecular weight than real one because of PS calibration. It is possible to determine a more accurate value using the ratio obtained comparing the molecular weight obtained for ***PDLLA-OH*** by SEC analysis and by ^{1}H NMR ($\frac{M_{n,SEC}}{M_{n,NMR}} = 1.69$). Thus, a molecular weight of $M_{n,\,calc.} = \frac{M_{n,SEC}}{1.69} = 49\,400\ \mathrm{g.mol^{-1}}$ was calculated for ***PDLLA_2***, close to the theoretical value.

In conclusion, two different polymers were synthesized with a good control of molecular weights even if dispersities are slightly high. Moreover, the functionalization of ***PDLLA-OH*** with a M_n 8400 g.mol^{-1} was achieved following a two steps process based on conjugation chemistry, leading to a *N*-hydroxysuccinimide ester poly(D,L-lactide) (***PDLLA_1***).

3.1.2. Bioglass nanoparticles

Stöber-derived bioglass nanoparticle synthesis is divided in two main steps: 1) the formation of initial silica nanoparticles obtained in basic pH conditions and 2) the incorporation of calcium in the silica network *via* a final calcination step in view to confer bioactivity to the resulting glass nanoparticles.

Bioglass nanoparticles (***BGNp***) with a binary composition (SiO_2-CaO, nominal molar ratio Si:Ca of 85:15) were synthesized following a modified Stöber process based on Greasley *et al.* procedure [36]. Firstly, and in agreement with the literature, this synthetic process of silica nanoparticles leads to spherical particles with well controlled diameters. Indeed, both TEM image processing (Figure 2-A and 2-B) and dynamic light scattering (Table S1) demonstrated narrow size distribution with respectively mean diameter of 164 ± 13 nm and 203 ± 3 nm, the difference being attributed to the overestimation as DLS measures hydrodynamic diameter and not particles diameter [35]. Considering the composition of BGNp, around 20 mol% of nominal calcium amount was effectively detected using ICP-OES analysis (Table S1). This value is in agreement with previous results [36]. Solid state NMR was carried out on such kind of nanoparticles before and after calcium addition (Figure 3-A). Beyond Q^4_{Si} (-110 ppm) and Q^3_H (-103 ppm) species that are present for both samples, a Q^2_{Ca} band (-83 ppm) is present for the second sample, meaning that calcium is well integrated in the silica network decreasing its connectivity: 3.5 *vs*. 3.0 (see supporting information for calculation and results in Table S2).

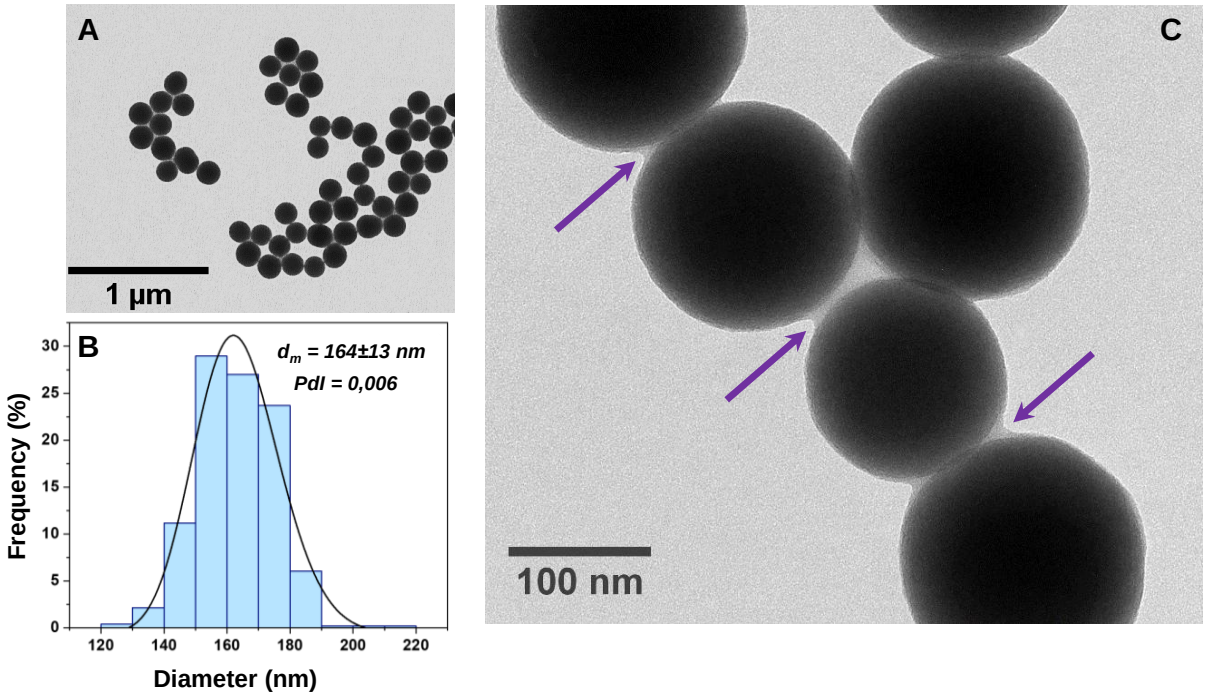

Figure 2. A) TEM image of bioglass nanoparticles (BGNp), B) BGNp size distribution and C) TEM image of PDLLA-grafted bioglass nanoparticles (BGNp-PDLLA_1), with arrows indicating polymer coronas interpenetration.

Several routes for synthesis of bioglass nanoparticles were described in the literature [41,42]. The first way is based on Stöber synthesis [36,43–45] for which monodisperse, non-agglomerated and homogenous nanoparticles of several hundred nanometers are obtained. Indeed, as calcium is added in a final step after aggregation of primary silica particles, it does not strongly affect the size and morphology of the final nano-object. However, for the same reasons, the amount of incorporated calcium remains quite low. On the contrary, in a second strategy, calcium is directly added in the initial solution and then almost fully integrated but resulting particles morphologies and sizes are poorly defined and more agglomerated [46–50]. Despite recent attempts using surfactant to combine both morphological and compositional properties, no real conclusive tests have been described so far. Consequently, in the present study, we choose the first way for different reasons. Firstly, in this work, parameters were set to obtain monodisperse Ca-containing Nps of several hundred nanometers in view of bone substitution applications; such Np diameters could prevent the particle uptake through biological membrane. Moreover, the use of well-defined nanoparticles allows an easier demonstration of the proof of concept for both polymer "grafting onto" strategy and further freeze-casting process. Finally, in the "bricks-and-mortar" approach, narrow distribution of particles diameters tends to minimize selective sedimentation during the elaboration process.

3.1.3. PDLLA-grafted bioglass nanoparticles

As mentioned previously [35], amino-functionalized BGNp were obtained by surface modification with APTES, to activate BGNp reactivity toward carboxylic ***PDLLA_1*** end-groups. Consequently, ***PDLLA_1*** chains were intended to be grafted onto ***BGNp*** surface by conjugation chemistry (Figure 1). The two surface functionalization steps were confirmed by the ζ-potential evolution, -20 ± 1, 18 ± 2 and 9 ± 1 mV respectively for ***BGNp***, amino-functionalized BGNp and ***BGNp-PDLLA_1***. The modification of the ζ-potential value before and after the first step can be explain by the modification of surface hydroxyl groups by APTES. After the polymer grafting, the carbonated backbone of the polymer being less polar than the previous function, the ζ-potential is logically decreased. Mean diameter of the resulting ***BGNp-PDLLA_1*** presents very low changes comparing to non-grafted ***BGNp*** as demonstrated by TEM studies (Table S1: ***BGNp****:* 164 ± 13 nm, ***BGNp-PDLLA_1***: 167 ± 14 nm). Interestingly, mean hydrodynamic diameter is strongly increased (Table S1: ***BGNp****:* 203 ± 3 nm, ***BGNp-PDLLA_1***: 2 528 ± 868 nm) and presents high polydispersity, already showing the inter-particular aggregation and then demonstrating the ability of particles to bond together *via* surface polymer entanglement or weak bonds creation between the chains of different particles. As a reminder, DLS measurements were carried out in Ethanol. The latter is a good solvent of BG

nanoparticles but not for PDLLA chains. Consequently, associated DLS measurements could shed light on the behavior of PDLLA-grafted nanoparticles during the freeze-casting process that gradually increase nanoparticle concentration and then aggregation.

The bonding ability of such nanosystems can be supported by TEM pictures (obtained on dried suspension, Figure 2-C) on which a homogeneous thin polymer corona can be observed all around the particles and creating connecting necks between particles (arrows on Figure 2-C). Furthermore, the grafting of ***PDLLA_1*** on the ***BGNp*** surface was confirmed by FTIR spectroscopy analysis (Figure 3-B). Indeed, whereas only silica bands were observed for BGNp (at 1 200, 1 100, 800, 476 cm^{-1}), additional band typical of PDLLA (1 760 cm^{-1}) is present on ***BGNp-PDLLA_1*** spectrum. The amount of grafted ***PDLLA_1*** was determined using a previously described quantification method based on TGA analysis and validated by FTIR band deconvolution [35]. The exact quantification process is precisely presented in supporting information. The determined quantity of ***PDLLA_1*** grafted was 0.65 ± 0.04 mmol (6.5 wt%), corresponding to a grafting density of 0.22 ± 0.02 ***PDLLA_1*** chains.nm^{-2}.

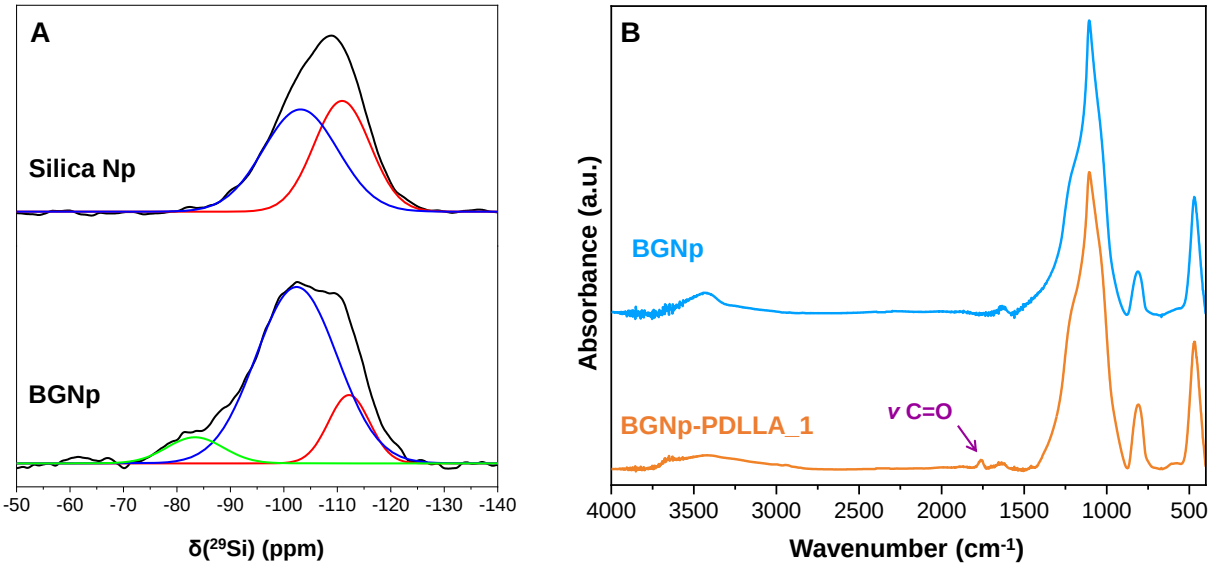

Figure 3. A) [29]Si CP-MAS NMR spectra of initial silica nanoparticles and bioglass nanoparticles with binary composition (SiO_2-CaO); B) FTIR spectra of bioglass nanoparticles (BGNp) and PDLLA-grafted bioglass nanoparticles (BGNp-PDLLA_1).

To conclude, this first description of PDLLA-grafted bioglass nanoparticle synthesis and associated characterizations are determinant as far as nanoparticle diameter, grafting density, molecular weight of grafted and free PDLLA used for scaffold elaboration are key factors to explain inter-particular interactions [51,52] and then mechanical cohesion of the final scaffolds.

3.2. Multiscale organization and mechanical properties of nanocomposite scaffolds

Nanocomposite macroporous scaffolds were elaborated combining "bricks-and-mortar" approach and freeze-casting process. Two working temperatures were used below solvent freezing temperature. Indeed, considering the literature [53–58], the most described tests are carried out with liquid nitrogen due to the ease of the process. However, using liquid nitrogen (-196°C) the resulting porosity size often appears too small for biological applications, and especially cell colonization. Consequently, a higher working temperature was chosen in order to evaluate the impact of temperature on the resulting porosity. Therefore, the samples presented in this work were respectively labelled S160 and obtained with a working temperature of T_W = -160 °C (in order to compare to the exiting temperature, using liquid nitrogen as cold source), and S10 with a working temperature of T_W = -10 °C (using a refrigerant bath as cold source). The latter temperature was fixed considering published [53] and unpublished preliminary tests.

3.2.1. Freeze-cast macroporous scaffolds structure

The elaborated scaffolds (Figure 4-A) measured 2.1 cm of diameter with a height of 1.1 cm and presented no shrinkage. The use of dimethyl carbonate as solvent during the freeze-casting process limit the conic shrinkage effects which are regularly observed for other solvents [53,59]. The resulting scaffolds showed different macroscopic aspect, confirming the effect of the working temperature on their appearance. The oriented macroporosity can already be observed for sample S10 on the top view and by transparence on the side one whereas on sample S160, no porosity can be distinguished.

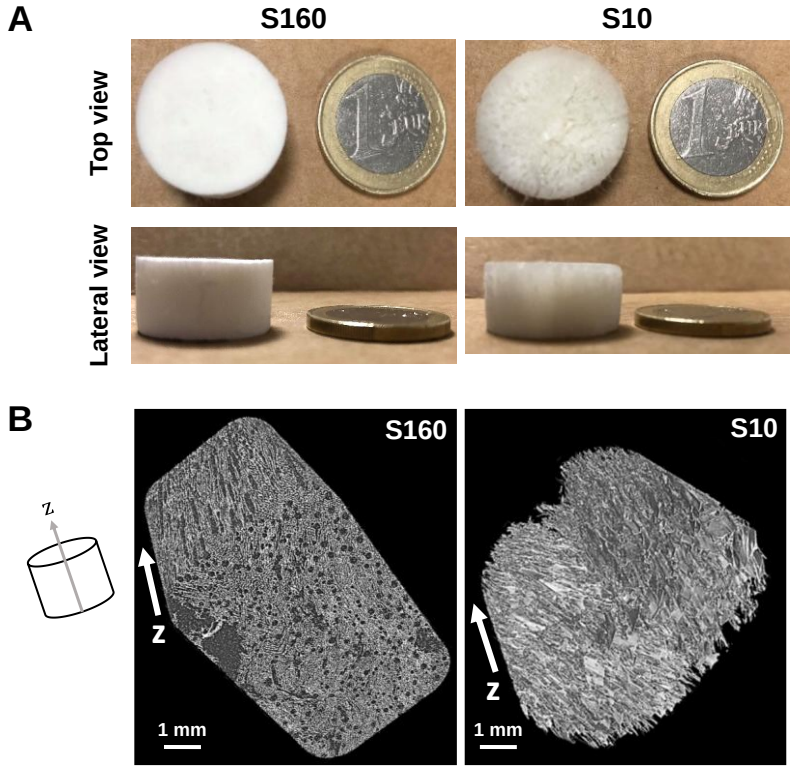

Figure 4. A) Optical images of nanocomposite macroporous scaffolds elaborated by freeze-casting; B) 3D µCT images of both S160 and S10 nanocomposite macroporous scaffolds (view from the bottom of the samples).

The porous structure of the two kinds of scaffolds was analyzed using X-ray microtomography (µCT). Firstly, the 3D views of the samples (Figure 4-B) showed an anisotropic macroporosity on volume of 4 x 4 x 8 mm, oriented along with the temperature gradient, as expected with the freeze-casting process [55,56]. Concerning the scaffold S160, two different types of porosity can be observed, the first type seems to present tubular shape whereas the second one corresponds to cellular morphology, with already described scale shape [14,60]. Contrary to S160, for sample S10, it was more difficult to distinguish tubular porosity from cellular one. The volume percent of porosity was evaluated on the totality of scaffolds and corresponded to 77 ± 3 % for S160 and to 94 ± 3 % for S10. The observation of the scaffolds top, median and bottom views highlighted the presence of a pore gradient along z-axis. Indeed, the size of porosity increased in the heat-transfer direction as demonstrated by video of slices along the z axis (videos available in supporting information). For each sample, the porosity size distribution was evaluated by image processing on 11 slices and on more than 50 000 pores of the median zone of the samples, using Feret diameter as comparison hypothesis (Figure S4). To remember, Feret diameter is defined as the distance between the two parallel lines, on opposite side, tangential to the object silhouette. It was used as reference size due to the limited resolution of the µCT images. The porous structure characteristics are listed in the Table 1. The results confirmed for S160 the presence of two types of porosity (Figure S5-A): the first one with a Feret diameter comprised between 30 and 50 µm and the second one with a mean Feret diameter of 188 ± 68 µm. Concerning the S10 sample, only one porosity size distribution was detected with a mean Feret diameter of 293 ± 55 µm (Figure S5-B).

Table 1. Porous structure characteristics determined both by µCT and SEM images analysis for S160 and S10 samples.

		S160		S10	
		µCT	***SEM***	***µCT***	***SEM***
Porosity	Volume percent (%)	77 ± 3	-	94 ± 3	-
	Surface percent (%)	-	82 ± 2	-	93 ± 1
Tubular porosity	D_F (µm)	188 ± 68	-	293 ± 55	-
	D_m (µm)	-	124 ± 22	-	-
Cellular porosity	D_F range (µm)	30 – 50	-	-	-
	L_m (µm)	-	105 ± 43	-	380 ± 55
	W_m (µm)	-	44 ± 17	-	190 ± 40

SEM observations of the top view and median section confirmed these analyses (Figure 5). In fact, for scaffold S160, the two porosity types can be observed whereas for S10, tubular porosity is toughly separable from cellular shaped pores. Qualitatively, pores are clearly larger on the top part of the scaffolds comparing to the median section (Figure 5). Image processing performed on the latter permits to determine both surface percent of porosity (on 3 images per sample), diameter of tubular porosity (when distinguishable) and mean length (L_m) and width (W_m) of cellular porosity (more than 30 pores/image). The obtained results are presented in the Table 1. The determined surface percent of porosity are respectively of 82 ± 2 % for S160 and 93 ± 1 % for S10. Like for µCT analysis, only scaffold S160 presented noticeable tubular porosity, with a mean diameter of 124 ± 22 µm. Concerning cellular porosity mean length and width, values are lower for scaffold S160 (L_m = 105 ± 43 µm, W_m = 44 ± 17 µm) than for S10 (L_m = 380 ± 55 µm, W_m = 190 ± 40 µm). All these results are consistent with µCT results in the same scaffold area. SEM images also allowed to estimate the wall thickness, showing thicker walls for S10 (7 ± 1 µm) than for S160 (4 ± 2 µm).

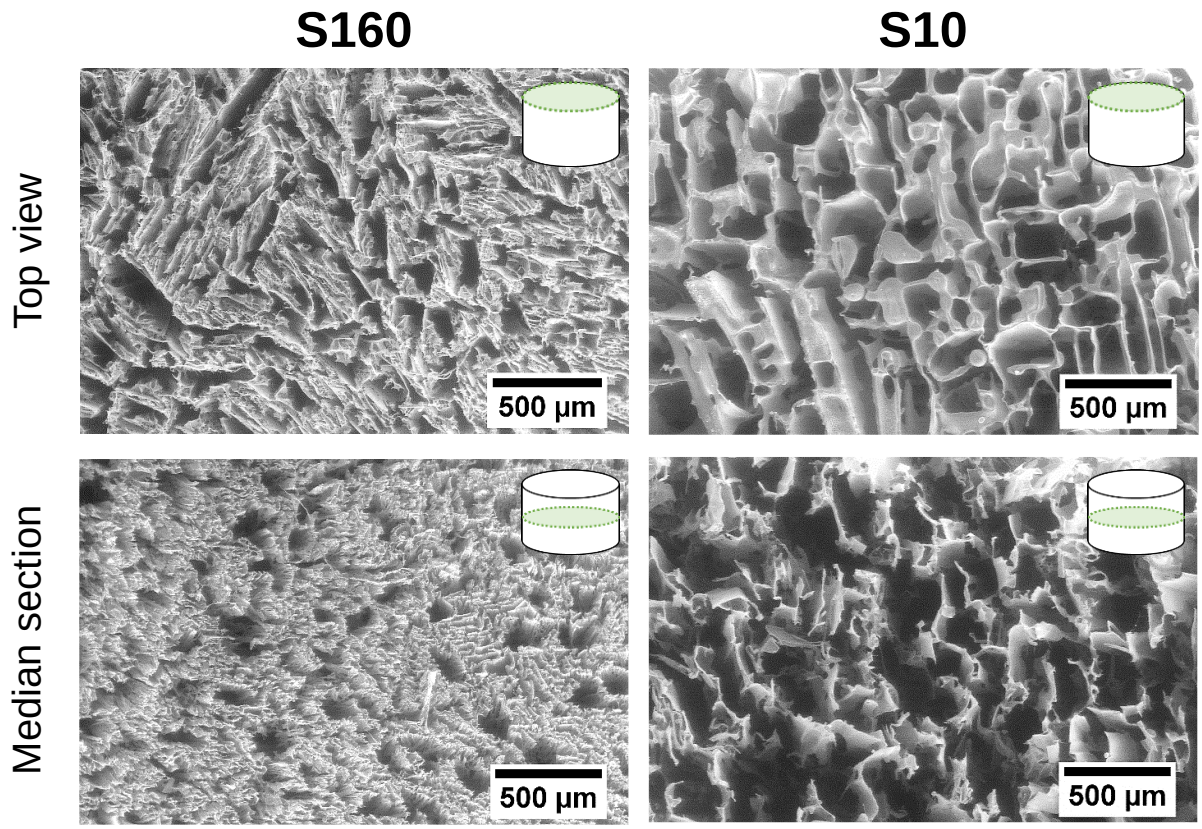

Figure 5. SEM images of top and median sections views of S160 and S10 scaffolds.

Finally, the pore size distribution and volume percent of porosity were characterized by mercury intrusion (Hg intrusion), corresponding curves and peaks are shown in Figure 6. For S160 sample, 3 peaks respectively centered around 108 ± 10 µm, 31 ± 10 µm and 3.8 ± 0.5 µm can be distinguished whereas only one intense peak is present around 146 ± 14 µm for sample S10, which is comparable with µCT and SEM derived results (Table 1). This analysis also intrinsically confirm that the scaffolds possess an open porosity.

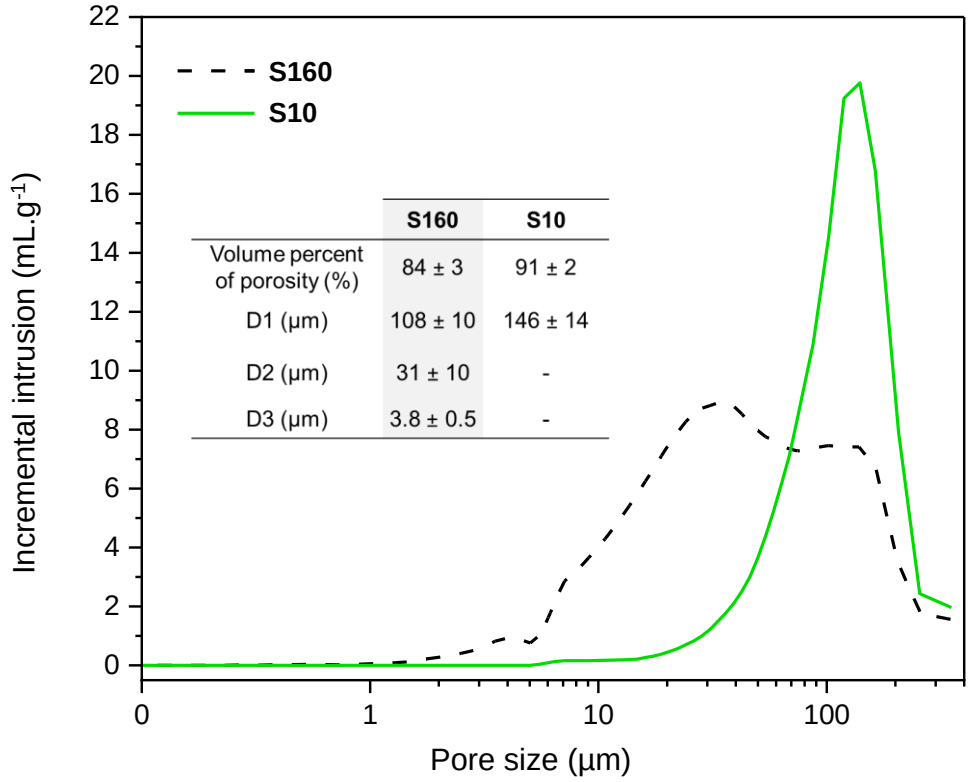

	S160	S10
Volume percent of porosity (%)	84 ± 3	91 ± 2
D1 (µm)	108 ± 10	146 ± 14
D2 (µm)	31 ± 10	-
D3 (µm)	3.8 ± 0.5	-

Figure 6. Pore size distribution determined by mercury intrusion for nanocomposite scaffolds S160 and S10 and resulting pore diameters.

The characterization of the macroporous structure of the elaborated scaffolds, both by µCT and SEM imaging, showed two morphologies of porosity, tubular and cellular, already described in the literature and specific to DMC use for thermally induced phase separation process (TIPS) [14,25,60–62]. Indeed, the planar structure of DMC molecule leads preferentially to the formation of planar crystals [59,63]. The two types of porosity can be explained by the crystal nucleation and growth phenomena. On one hand, the tubular macroporosity seems to be created by crystals merging together, just after the initial nucleation, inducing larger crystals. The cellular porosity, on the other hand, appears to be provoked by intercrystalline nucleation phenomenon, directly inside the solute-rich phase and binding tubular pores together. The volume percent of porosity, determined thanks to µCT scans and Hg intrusion (Table 1 and Figure 6), allowed to demonstrate a real impact of process working temperature on the total porosity of the resulting scaffolds. In fact, the more the temperature is close to the solvent fusion temperature ($T_{f,\,DMC}$ = 2-4 °C), the more the crystal growth is favored at the expense of the nucleation phenomenon, leading to larger DMC crystals and thus larger pores. Even if SEM imaging analysis of median sections only permitted to determine surface percent porosity, the obtained values are consistent with volume percent porosity (µCT and Hg intrusion), supposing that 2D analyses can be transposed to 3D ones. Moreover, concerning scaffolds S160, the results are close from the one presented in the literature for PDLLA/bioglass® scaffolds elaborated by TIPS with DMC at a lower temperature (-196 °C) [60,64,65]. Regarding porosity size, the range and mean diameters characterized by the three different techniques (Table 1 and Figure 6) showed an important difference of pore size between S160 and S10 samples, confirming that the working temperature is a key parameter to control the macroporous structure. Indeed, scaffolds S160 elaborated with T_W = -160 °C led to pores with a mean diameter of about 100-200 µm, the size range determined for those scaffolds is consistent with data presented in the literature for samples elaborated by TIPS in liquid nitrogen [60,64,65]. However, the pore size of S160 scaffolds seems to be too thin comparing to the requested pore size described in the literature for cell colonization and growth, particularly for bone reconstruction [66]. On the contrary, S10 scaffolds prepared at T_W = -10 °C exhibited mean pore size around 300-400 µm, which corresponds to targeted range for cell colonization in biomedical applications an especially for bone substitution[66] (150-500 µm). Concerning walls thickness, the presence of thicker walls for S10 scaffolds comparing to S160 scaffolds, is linked to nucleation and crystal growth phenomenon. In fact, for T_W = -10 °C,

the higher temperature gradient leads to a slowly solidification rate and favors the crystals growth and their merging, letting more time to the solid phase to be repelled in thicker intercrystalline spaces and thus thicker pore walls. Finally, the results of mercury intrusion are coherent with µCT and SEM images analysis; the small differences can be explained by both the limit of detection of the device (detections of pores smaller than 150 µm) and the calculation hypothesis of cylindrical pores. They also emphasized the presence of small porosity (4 µm) for scaffolds S160. This porosity, observed in pore walls (Figure S6, Figure 9), seems to be induced by both undercooling phenomenon and by solvent entrapment between polymer chains during the solidification, resulting to porosity formation during sublimation process. Such kind of small macroporosity is particularly interesting to be used as potential "microtanks" to store growth factors and locally high ions concentration to stimulate cells, enhance supersaturation and then apatite and new bone formation [67]. S10 samples do not exhibit this sort of wall porosity, the lower temperature gradient seems to allow the solid phase to rearrange slowly in intercrystalline spaces and to limit solvent entrapment and undercooling effects.

To complete the analysis of the macroporous scaffolds, µCT and SEM observations were performed on the slice of the samples. For the two types of samples, a structural gradient can be observed on both the top, median and bottom µCT (Figure S4) sections and on µCT and SEM slice views (Figure 7). In fact, the bottom areas directly in contact with the cold finger are denser and present numerous small pores comparing to higher zones. This phenomenon has already been described for macroporous materials elaborated by TIPS or freeze casting [55,56]. It is mainly explained by a high initial solidification rate when the mold enters in contact with the cold finger, leading to a planar initial solidification front, which tends to trap solute in crystals [68]. The conditions at the beginning of the solidification are more favorable for crystals nucleation than growth. Then once the solidification rate is stabilized, crystals propagation and growth are kinetically favored. Furthermore, the larger pore size at the top of the samples seems to be induced by the formation of solvent crystals. In fact, the solvent crystals form an insulation layer, limiting the solidification rate after a certain height. The decrease of the solidification rate thus affects the size of the pores, creating larger crystals. Beyond this structural gradient, the slice observations by µCT and SEM of both samples show an anisotropic lamellar porosity oriented along the z-axis, corresponding to the temperature gradient direction. These results confirm the orientation of the porosity thanks to the solidification front direction using freeze-casting process and demonstrate the presence of interconnected and open porosity throughout the scaffold, necessary for cell colonization and angiogenesis. Beyond this macroporous network, that is adapted for bone regeneration, preliminary experiments have been carried out in SBF to test the bioactivity of the scaffolds (Figure S7). After 7 days of immersion at 37 °C, X-Ray diffraction and SEM analysis done on the immersed materials validate the formation of precipitates composed of aggregated poorly crystallized apatite crystals on the surface of S10 scaffolds and demonstrate the ability of such scaffolds to form bone-like minerals *in vitro*.

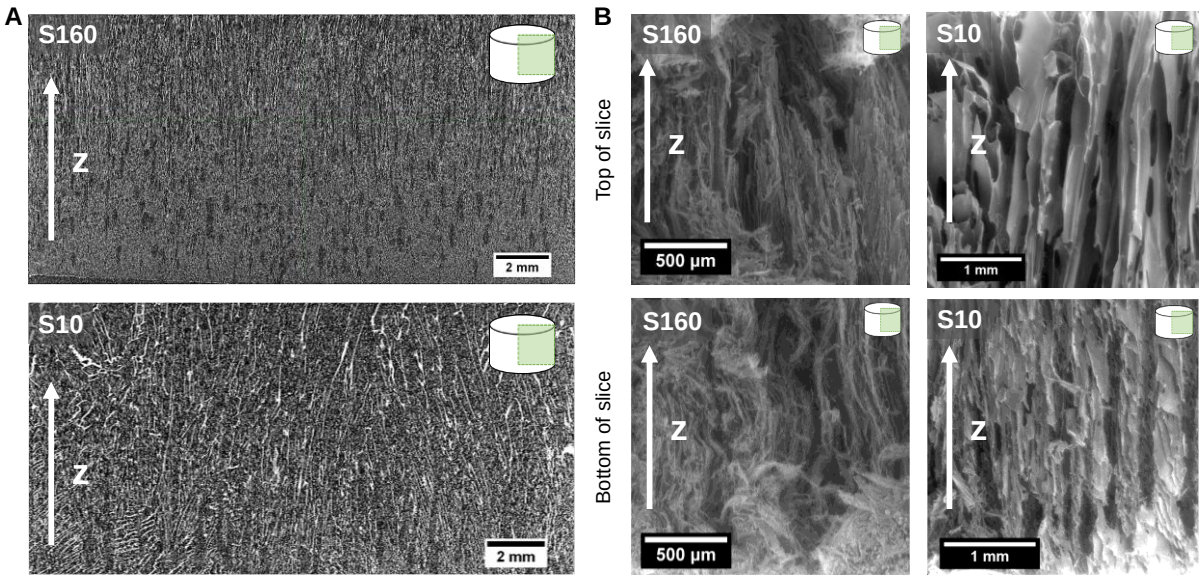

Figure 7. A) µCT slices images of S160 and S10 scaffolds and B) SEM observations of the corresponding top and bottom of scaffold slices.

3.2.2. *Influence of the freeze-casting working temperature on mechanical properties: the role of the macroporous structure*

The compressive behavior of porous cellular materials is highly dependent on their porosity, pore size and morphology but also on wall thickness. Even if both scaffolds possess anisotropic porosity oriented along z-axis, giving them orthotropic properties, their porosity and their pore size are significantly different. So, in order to evaluate the effect of the porous structure of the scaffolds and thus the working temperature on their mechanical properties, uniaxial mechanical compression tests were carried out on z-axis. As explained previously, measurements were run in triplicate and a very low dispersion was noticed between the 3 samples, confirming the freeze-casting process reproducibility. A representative curve of the results obtained for each of the two materials is shown on Figure 8-A. The expected response for this type of porous cellular material consists of three steps: a nearly linear elastic regime followed by an extensive load plateau ending with the final densification. Depending on the size of the smallest closed pores and on the thickness of their walls, this plateau can have a more or less steep slope [69].

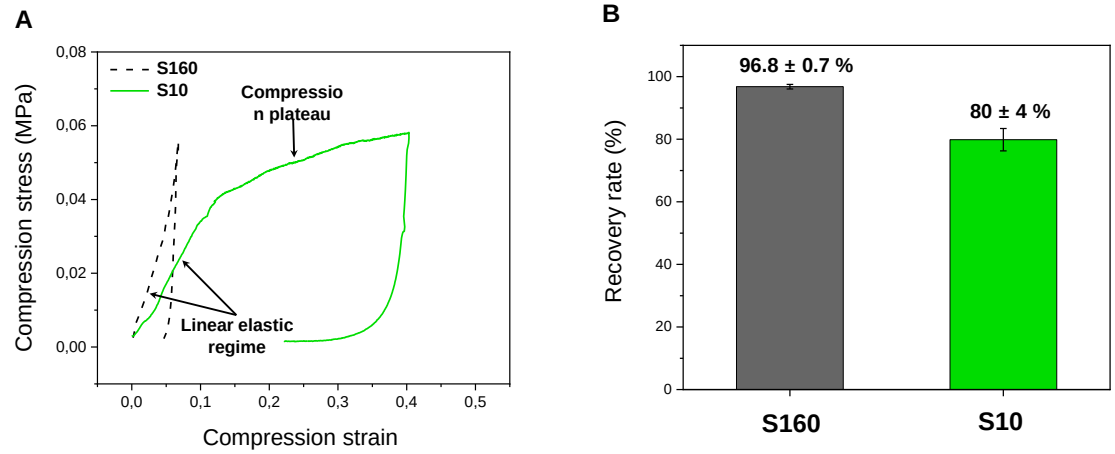

Figure 8. Mechanical properties of scaffolds S160 and S10: A) uniaxial stress-strain curves and B) recovery rates 24 hours after uniaxial compressive test.

In these tests, the maximal load of 20 N corresponds to a 0.058 MPa compression. This value is representative of the intended application and does not allow for a complete exploration of the compressive behavior. However, the initial nearly elastic step was characterized and used to determine a compressive

modulus. The compressive modulus value of S160 (E_{S160} = 1.32 ± 0.01 MPa) was significantly higher than for S10 (E_{S10} = 0.37 ± 0.05 MPa). If S160 scaffolds are stiffer during the initial elastic step, their compression curve quickly shows a break in slope. For the targeted compressive stress, the strain was considerably larger for scaffolds S10 (ε_{max} = 0.47 ± 0.07) than for scaffolds S160 (ε_{max} = 0.07 ± 0.01). These results clearly confirm that the porous structure, induced by the working temperature, affects the mechanical properties. The S160 scaffolds presented small and numerous pores, involving a more important number of walls comparing to S10 scaffolds. Smaller cell sizes limit the elastic instability on the one hand, and on the other hand, the stress is distributed more homogeneously [69]. The compressive modulus determined for S160 scaffolds is close to results presented in the literature for PDLLA/Bioglass® scaffolds elaborated by freeze-casting with a lower nanoparticle loading rate and higher polymer concentration (1.2 ± 0.4 MPa) [65]. Such similar compressive modulus, 1.7 MPa, was also found for freeze-cast scaffolds based on cross-linked gelatin and bioglass nanoparticles (50 wt%) with similar pore size (100-200 µm) [70]. Concerning S10 scaffolds, they possessed a lower compressive modulus, mainly linked with a larger porosity and larger pore size. Although their cell walls are thicker than S160 ones and the PDLLA-grafted nanoparticles may stiffen them by limiting the mobility of the polymer chains, these effects are insufficient in regards to the S10 porosity of 91%, higher than the 84% of S160. This also explains their larger maximal deformation: porous cells collapse progressively leading to wall buckling and modifying scaffold shape. Bossard *et al*. obtained comparable compressive modulus (0.49 ± 0.03 MPa) for hybrids PCL/bioglass (up to 40 wt% of bioglass) scaffolds with a pore size range of 300-500 µm [9]. The compressive modulus of elaborated scaffolds are significantly below those of trabecular bones (0.6-2.1 GPa) [71], however, this should not be a major concern for use in non-weight bearing bones. In fact, the scaffolds are intended to resorb gradually as new bone grows, leading to an improvement of mechanical properties

Finally, the scaffold dimensions were measured 24 hours after the compressive mechanical tests in order to evaluate their capacity of recovery in height. The results, presented in the Figure 8-B, indicated that scaffolds S160 possessed a better recovery rate, 96.8 ± 0.7 %, than scaffolds S10, 80 ± 7 %. These values clearly highlight the predominantly viscoelastic behavior of the two materials. S160 excellent recovery indicates that only little irreversible strain or damage occurred during the 20 N compression test and that the walls buckling was mainly reversible. As seen before, S10 scaffolds had larger and fewer pores than S160, which might induce more irreversible processes (plastic strain and damage). Both recovery rates stay interesting for biomedical application, indeed, during biomaterials implantation, surgeons often need to force to place the implant properly.

3.2.3. Effect of bioglass nanoparticles functionalization with polymer chains

The "bricks-and-mortar" concept used in this work is based on the formation of link between the *bricks*, herein the bioglass nanoparticles, thanks to the presence of polymer covalently grafted at their surface and free polymer chains, the *mortar* [32,33,72]. With the aim to investigate the role of bioglass nanoparticles functionalization, two kind of scaffolds (respectively S10 and $S_{NG}10$) were processed at -10°C from solution containing either polymer-grafted nanoparticles (***BGNp-PDLLA_1***) and free polymer (***PDLLA_2***) or non-grafted nanoparticles (***BGNp***) and free polymer (***PDLLA_2***) (see part 2.3.1 and 2.3.2). Even if the main compressive curves (Figure S8) are a slightly different, the resulting mean values (evaluated on 3 scaffolds) of compressive modulus (E_{S10} = 0.37 ± 0.05 MPa, E_{SNG10} = 0.31 ± 0.03 Mpa) and maximal compressive strain (ε_{max} ($S_{NG}10$) = 0.5 ± 0.1, ε_{max} (S10) = 0.47 ± 0.07) are comparable (Table S3 and Figure S9). These results highlight that the global compressive behavior of freeze-cast scaffolds is mainly driven by their porous structure independently of the nanoparticle functionalization. However, height recovery rates of S10 and $S_{NG}10$ scaffolds significantly differ, respectively 80 ± 4 % for S10 and 72 ± 6 % for $S_{NG}10$. It indicates that the $S_{NG}10$ scaffolds present a more important part of irreversible deformation (plastic strain and damage) than the S10 scaffolds.

An inhomogeneous repartition of the nanoparticles and the presence of agglomerates can explain this lower recovery rate for $S_{NG}10$ scaffolds. In fact, the presence of fillers generally stiffens the pore walls limiting polymer chains mobility and thus pore walls collapsing. Nevertheless, inhomogeneous distribution in the height of scaffolds could create defects and ununiform mechanical behavior with irreversible failures concentrated in a part of the samples. In order to evaluate this hypothesis, the spatial distribution of fillers was studied at different scales. First SEM images (Figure 9) show bigger agglomerates for both samples in

the bottom part of the slice due to the equilibrium of the solidification front during the freeze-casting process. However, $S_{NG}10$ scaffolds presents larger agglomerates than the S10. Concerning the middle and top part of the slices, $S_{NG}10$ scaffolds still possess large particles agglomerates inside the pore walls, with a really few amounts of inorganic fillers in the top part comparing to the middle and bottom ones. In contrary, the S10 samples images show homogeneously distributed small aggregates in the walls of the middle and top parts of the slice. Consequently, these images confirm that the PDLLA-grafted nanoparticles are more homogeneously distributed in all the height of the scaffolds rather than the non-grafted nanoparticles tend to form large agglomerates and to remain in the lower part of the scaffolds, creating weakness in the sample like confirmed by the mechanical study.

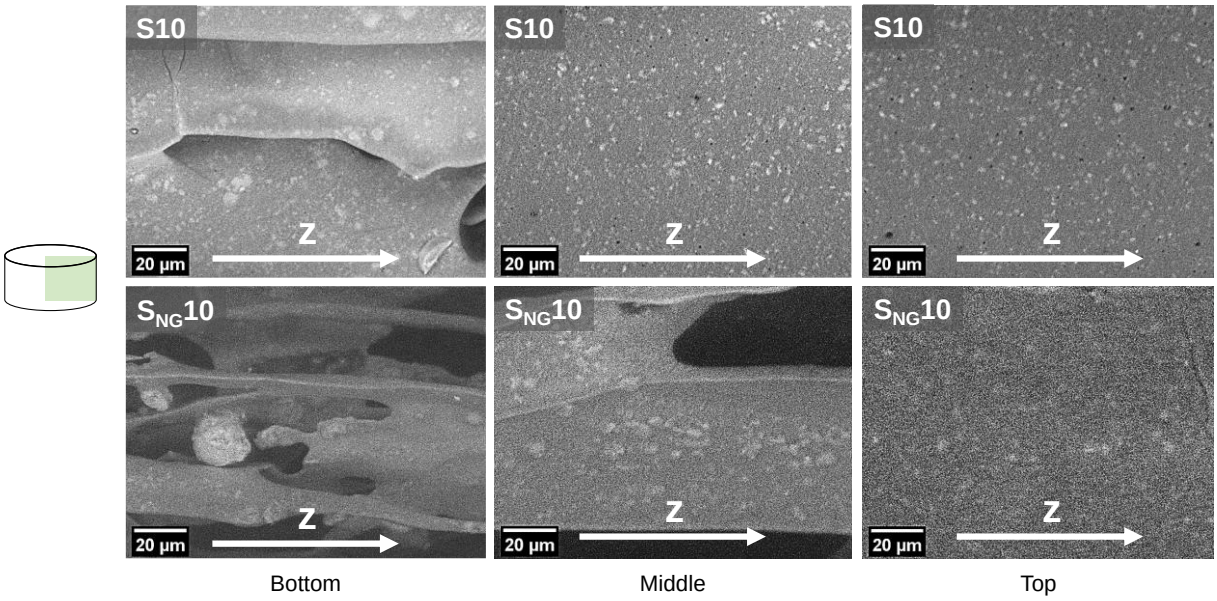

Figure 9. SEM (backscattering mode) observations of fillers aggregates on the top, middle and bottom parts of scaffold slices.

Complementary FEG-SEM characterization were performed on the middle of slices for both samples S10 and $S_{NG}10$. The bioglass nanoparticles are clearly seen in white, embedded in the polymer matrix in grey (Figure 10-A and B). For both samples, a systematic tangency of the bioglass nanoparticles is noticed. Nevertheless, whereas nanoparticles tend to form homogeneously distributed and embedded rosaries-like chains for S10 samples (Figure 10-C and E), their cohesion appear to be low in the aggregation zones for the $S_{NG}10$ samples (Figure 10-D and F), leading to poor local mechanical properties. The proximity and formation of rosaries in the slice of S10 scaffolds, should be induced by polymer chains entanglement and weak bonds formation between PDLLA-grafted chains and free PDLLA chains [51,52]. For S10 samples, the homogeneous nanoparticle density and distribution both along the scaffold height and at a micron-scale tend to confirm the validity of the "bricks-and-mortar" concept. Chevigny *et al*. showed that the molecular weight ratio between grafted polymer chains and free polymer chains has an important influence on chains entanglement and interactions [51,52]. Indeed, to promote free chains interpenetration in the polymer-grafted corona, the free chains molecular weight should be lower or close to the one of grafted chains. This is an attractive prospect for the continuation of the present work. Our results clearly demonstrate the correlation between nanoparticle functionalization and mechanical properties, especially the recovery rate that is predominant to prevent porosity collapse during handling and cutting steps before implantation. Thus, adjusting nanoparticle size, free polymer chains and/or grafted polymer chains molecular weight, leading to better mechanical properties, could improve the repartition of the PDLLA-grafted nanoparticles. Beyond mechanical properties, limitation of aggregates size and numbers would ensure spatial standardized degradation of scaffolds and limit burst effect.

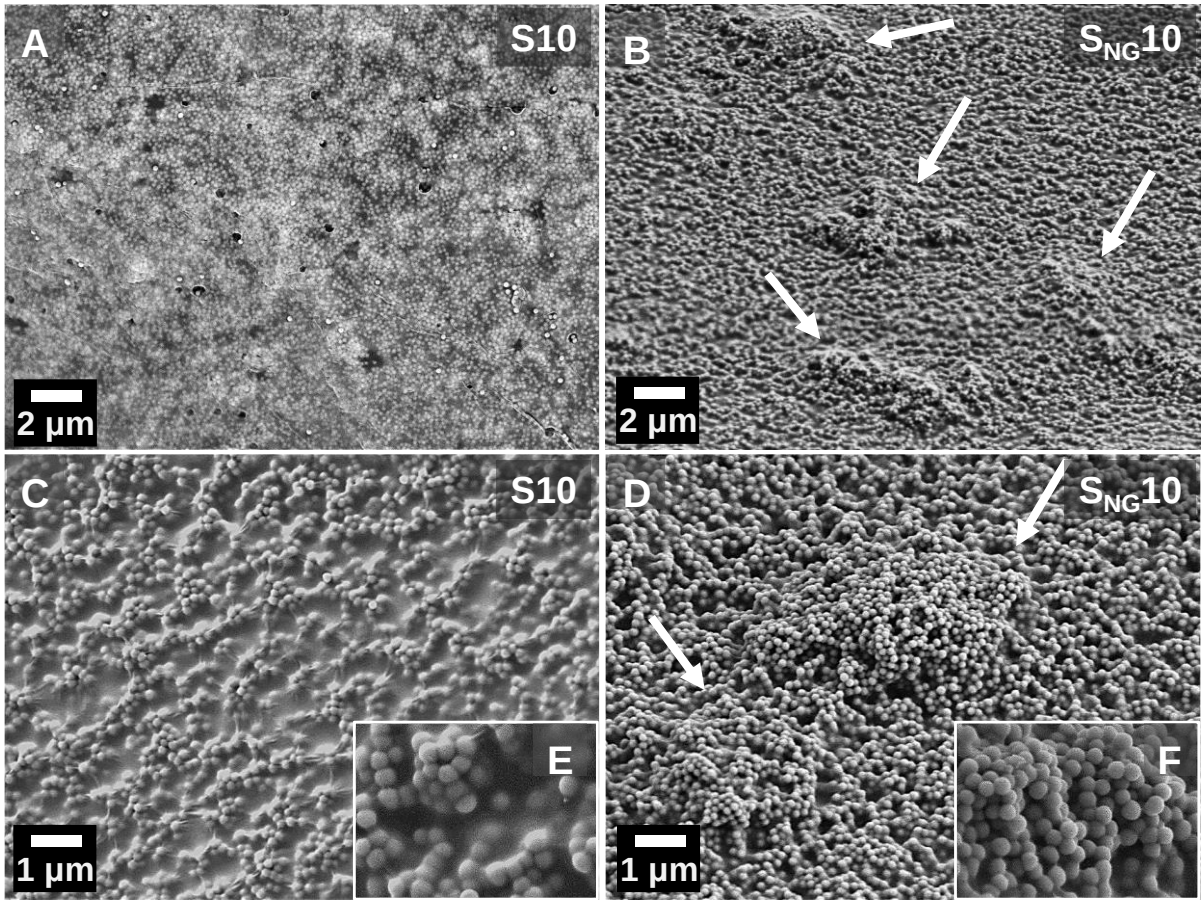

Figure 10. FEG-SEM observations of pore walls median zone with two magnifications on S10 and $S_{NG}10$ scaffolds slice. White arrows designate micron-scale agglomerates.

4. CONCLUSION

This study demonstrated for the first time a new way for the fabrication of bioactive glass/polyester nanocomposite scaffolds, combining "bricks-and-mortar" concept and freeze-casting. This integrative approach, from the synthesis of well-defined functionalized poly(D,L-lactide) and bioactive glass nanoparticles and their subsequent grafting, to their organization into macroporous scaffolds has been validated at each step thanks to multiscale characterization. Indeed, nanoparticle diameter, molecular weight of grafted and free PDLLA used for scaffold elaboration are key factors to explain inter-particular interactions and then mechanical properties. This hypothesis was confirmed by the proximity and formation of particles rosaries induced by polymer chains entanglement and weak bonds formation between PDLLA-grafted chains and free PDLLA chains. This phenomenon leads to highly homogeneous spatial distribution of nanoparticles at the scale of walls and directly prevents sedimentation of inorganic fillers. Depending on the freezing temperature, the shrinkage-free centimeter-scale scaffolds presented bimodal porosity from a few microns to several hundred microns with different morphologies (cellular *vs* tubular) and high porosity volume percent. These results corroborated the orientation of the porosity thanks to the solidification front direction using freeze-casting process and demonstrated the presence of interconnected and open porosity, necessary for cell colonization and angiogenesis. The compressive modulus values from 0.37 to 1.32 MPa are adapted for non-loaded sites and clearly confirm that the porous structure and pore wall thickness induced by the working temperature, strongly affect the mechanical properties. These elastic compressive moduli are close to results presented in the literature for freeze-casting-derived polyester/bioactive glass scaffolds, but presenting lower inorganic filler loading rate whereas the latter are predominant to enhance bioactivity and bone new formation.

These mechanical properties could be improved either by tuning the ratio between the chain length of free and grafted polymer or by grafting polymer chains with higher molecular weight. Further experiments (some already in process) such as systematic acellular *in vitro* degradation tests (TRIS and/or SBF), cellular cytotoxicity and mineralization *in vitro* assays and *in vivo* studies are necessary to validate the biological potential of such materials. However, the results presenting in this article open up interesting perspectives

or improvements, as the biological properties can be tuned using the integrative approach, the latter allowing to isolate each elaboration step from the suspension formulation (bioactive glass nanoparticles composition and diameter, molecular weight ratio between grafted polymer chains and free polymer chains) to the scaffold fabrication parameters (working temperature).

CREDIT AUTHORSHIP CONTRIBUTION STATEMENT

P. Lagarrigue: Investigation, Methodology, Validation, Writing - Original draft
V. Darcos: Co-supervision, Conceptualization, Methodology, Resources, Project administration, Funding acquisition, Writing - Original draft
C. Tenailleau: Investigation, Writing - Review & Editing
B. Duployer: Investigation
A. Dupret-Bories: Writing - Review & Editing
S. Cazalbou: Investigation, Writing - Review & Editing
D. Poquillon: Methodology, Validation, Writing - Review & Editing
D. Grossin: Methodology, Validation, Writing - Original draft
C. Combes: Co-supervision, Validation, Project administration, Funding acquisition, Writing - Original draft
J. Soulié: Co-supervision, Conceptualization, Validation, Resources, Methodology, Project administration, Funding acquisition, Writing – Original draft

DECLARATION OF COMPETING INTEREST

The authors declare that they have no known competing financial interests or personal relationships that could have appeared to influence the work reported in this paper.

ASSOCIATED CONTENT

Additional supporting information may be found in the online version of this article.

Freeze-casting device representative scheme and explanations, polymer synthetic pathway and characterization, bioglass nanoparticles and PDLLA-grafted bioglass nanoparticles complementary characterizations (DLS analysis, ζ-potential measurements, specific surface area measurements, chemical composition, network connectivity, thermogravimetric analysis), characterization of the porous structure of the scaffolds by μCT (bottom, median and top views, distribution of Feret diameters of median views and link to the videos of reconstruction) and SEM, bioactivity tests in SBF and evaluation of the effect of polymer grafting on scaffolds mechanical properties (uniaxial stress-strain curves, mechanical properties, recovery rates).

ACKNOWLEDGMENTS

The authors thank the SynBio3 platform (IBMM, Montpellier) for the SEC analyses, Raimond Castaing Microcaracterisation Center and in particular Alessandro Pugliara and Stephane Le Blond Duplouy for TEM and FEG-SEM analyses and Yannick Coppel from LCC for solid state NMR analyses. The French FERMaT Federation FR3089 is acknowledged for providing X-ray tomography laboratory facility.

FUNDING

The Institut Carnot Chimie Balard Cirimat (ANR-16-CARN-0008-01) and ANR CongOs (ANR-20-CE19-0019) supported this work.

REFERENCES

(1) Lagarrigue, P.; Soulié, J.; Chabrillac, E.; Darcos, V.; Grossin, D.; Vergez, S.; Combes, C.; Dupret-Bories, A. Biomaterials and Osteoradionecrosis of the Jaw: Review of the Literature According to the SWiM Methodology. *Eur. Ann. Otorhinolaryngol. Head Neck Dis.* **2021**, S187972962100140X. https://doi.org/10.1016/j.anorl.2021.06.006.
(2) Hutmacher, D. W. Scaffolds in Tissue Engineering Bone and Cartilage. *Biomaterials* **2000**, *21*, 2529–2543. https://doi.org/10.1016/S0142-9612(00)00121-6.

(3) Hench, L. L. The Story of Bioglass. *Journal of materials science. Materials in medicine* **2006**, *17* (11), 967–978. https://doi.org/10.1007/s10856-006-0432-z.
(4) Reffitt, D. M.; Ogston, N.; Jugdaohsingh, R.; Cheung, H. F. J.; Evans, B. A. J.; Thompson, R. P. H.; Powell, J. J.; Hampson, G. N. Orthosilicic Acid Stimulates Collagen Type 1 Synthesis and Osteoblastic Differentiation in Human Osteoblast-like Cells in Vitro. *Bone* **2003**, *32* (2), 127–135. https://doi.org/10.1016/S8756-3282(02)00950-X.
(5) Jones, J. R. Review of Bioactive Glass: From Hench to Hybrids. *Acta biomaterialia* **2013**, *9* (1), 4457–4486. https://doi.org/10.1016/j.actbio.2012.08.023.
(6) Valerio, P.; Pereira, M. M.; Goes, A. M.; Leite, M. F. Effects of Extracellular Calcium Concentration on the Glutamate Release by Bioactive Glass (BG60S) Preincubated Osteoblasts. *Biomedical Materials* **2009**, *4* (4). https://doi.org/10.1088/1748-6041/4/4/045011.
(7) Hoppe, A.; Güldal, N. S.; Boccaccini, A. R. A Review of the Biological Response to Ionic Dissolution Products from Bioactive Glasses and Glass-Ceramics. *Biomaterials* **2011**, *32* (11), 2757–2774. https://doi.org/10.1016/j.biomaterials.2011.01.004.
(8) Valliant, E. M.; Jones, J. R. Softening Bioactive Glass for Bone Regeneration: Sol–Gel Hybrid Materials. *Soft Matter* **2011**, *7* (11), 5083. https://doi.org/10.1039/c0sm01348j.
(9) Bossard, C.; Granel, H.; Wittrant, Y.; Jallot, É.; Lao, J.; Vial, C.; Tiainen, H. Polycaprolactone / Bioactive Glass Hybrid Scaffolds for Bone Regeneration. *Biomedical Glasses* **2018**, *4* (1), 108–122. https://doi.org/10.1515/bglass-2018-0010.
(10) Mota, J.; Jansen, J. A.; Mano, J. F.; Yu, N.; Luz, G. M.; Caridade, S. G.; Gomes, M. E.; Reis, R. L.; Walboomers, X. F. Chitosan/Bioactive Glass Nanoparticle Composite Membranes for Periodontal Regeneration. *Acta Biomaterialia* **2012**, *8* (11), 4173–4180. https://doi.org/10.1016/j.actbio.2012.06.040.
(11) Srinivasan, S.; Jayasree, R.; Chennazhi, K. P.; Nair, S. V.; Jayakumar, R. Biocompatible Alginate/Nano Bioactive Glass Ceramic Composite Scaffolds for Periodontal Tissue Regeneration. *Carbohydrate Polymers* **2012**, *87* (1), 274–283. https://doi.org/10.1016/j.carbpol.2011.07.058.
(12) Arcos, D.; Ragel, C. V.; Vallet-Regí, M. Bioactivity in Glass/PMMA Composites Used as Drug Delivery System. *Biomaterials* **2001**, *22* (7), 701–708. https://doi.org/10.1016/S0142-9612(00)00233-7.
(13) Vergnol, G.; Ginsac, N.; Rivory, P.; Meille, S.; Chenal, J. M.; Balvay, S.; Chevalier, J.; Hartmann, D. J. In Vitro and in Vivo Evaluation of a Polylactic Acid-Bioactive Glass Composite for Bone Fixation Devices. *Journal of Biomedical Materials Research - Part B Applied Biomaterials* **2016**, *104* (1), 180–191. https://doi.org/10.1002/jbm.b.33364.
(14) Boccaccini, A. R.; Maquet, V. Bioresorbable and Bioactive Polymer/Bioglass?? Composites with Tailored Pore Structure for Tissue Engineering Applications. *Composites Science and Technology* **2003**, *63* (16), 2417–2429. https://doi.org/10.1016/S0266-3538(03)00275-6.
(15) Li, H.; Chang, J. PH-Compensation Effect of Bioactive Inorganic Fillers on the Degradation of PLGA. *Composites Science and Technology* **2005**, *65* (14), 2226–2232. https://doi.org/10.1016/j.compscitech.2005.04.051.
(16) Renders, G. A. P.; Mulder, L.; van Ruijven, L. J.; van Eijden, T. M. G. J. Porosity of Human Mandibular Condylar Bone. *Journal of Anatomy* **2007**, *210* (3), 239–248. https://doi.org/10.1111/j.1469-7580.2007.00693.x.
(17) Koh, Y.-H.; Kim, H.-W.; Kim, H.-E.; Jang, J.-H.; Shin, D.-S.; Jo, J.-H.; Lee, E.-J. In Vitro / in Vivo Biocompatibility and Mechanical Properties of Bioactive Glass Nanofiber and Poly(ε-Caprolactone) Composite Materials. *Journal of Biomedical Materials Research Part B: Applied Biomaterials* **2009**, *91B* (1), 213–220. https://doi.org/10.1002/jbm.b.31392.
(18) Cannillo, V.; Chiellini, F.; Fabbri, P.; Sola, A. Production of Bioglass® 45S5 - Polycaprolactone Composite Scaffolds via Salt-Leaching. *Composite Structures* **2010**, *92* (8), 1823–1832. https://doi.org/10.1016/j.compstruct.2010.01.017.
(19) Serra, T.; Planell, J. A.; Navarro, M. High-Resolution PLA-Based Composite Scaffolds via 3-D Printing Technology. *Acta Biomaterialia* **2013**, *9* (3), 5521–5530. https://doi.org/10.1016/j.actbio.2012.10.041.
(20) Georgiou, G.; Mathieu, L.; Pioletti, D. P.; Bourban, P.-E.; Månson, J.-A. E.; Knowles, J. C.; Nazhat, S. N. Polylactic Acid–Phosphate Glass Composite Foams as Scaffolds for Bone Tissue Engineering. *J. Biomed. Mater. Res.* **2007**, *80B* (2), 322–331. https://doi.org/10.1002/jbm.b.30600.
(21) Baldino, L.; Aragón, J.; Mendoza, G.; Irusta, S.; Cardea, S.; Reverchon, E. Production, Characterization and Testing of Antibacterial PVA Membranes Loaded with HA-Ag_3PO_4 Nanoparticles, Produced by SC-CO_2 Phase Inversion: Production and Testing of Antibacterial PVA Membranes Produced by SC-CO_2 Process. *J. Chem. Technol. Biotechnol.* **2019**, *94* (1), 98–108. https://doi.org/10.1002/jctb.5749.

(22) Wang, Z.; Zhao, S.; Hong, L.; Huang, J. Preparation and Properties of Silver-Based Cellulose/Polyvinyl Alcohol Antibacterial Materials. *J Inorg Organomet Polym* **2020**, *30* (11), 4382–4393. https://doi.org/10.1007/s10904-020-01669-5.
(23) Deville, S. The Lure of Ice Templating: Recent Trends and Opportunities for Porous Materials. *Scripta Materialia* **2018**, *147*, 119–124. https://doi.org/10.1016/j.scriptamat.2017.06.020.
(24) Day, R. M.; Maquet, V.; Boccaccini, A. R.; J??r??me, R.; Forbes, A. In Vitro and in Vivo Analysis of Macroporous Biodegradable Poly(D,L-Lactide-Co-Glycolide) Scaffolds Containing Bioactive Glass. *Journal of Biomedical Materials Research - Part A* **2005**, *75* (4), 778–787. https://doi.org/10.1002/jbm.a.30433.
(25) Boccaccini, a. R.; Blaker, J. J.; Maquet, V.; Day, R. M.; Jérôme, R. Preparation and Characterisation of Poly(Lactide-Co-Glycolide) (PLGA) and PLGA/Bioglass® Composite Tubular Foam Scaffolds for Tissue Engineering Applications. *Materials Science and Engineering: C* **2005**, *25* (1), 23–31. https://doi.org/10.1016/j.msec.2004.03.002.
(26) Maquet, V.; Boccaccini, a. R.; Pravata, L.; Notingher, I.; Jérôme, R. Porous Poly(α-Hydroxyacid)/Bioglass® Composite Scaffolds for Bone Tissue Engineering. I: Preparation and in Vitro Characterisation. *Biomaterials* **2004**, *25* (18), 4185–4194. https://doi.org/10.1016/j.biomaterials.2003.10.082.
(27) Blaker, J. J.; Maquet, V.; Jérôme, R.; Boccaccini, A. R.; Nazhat, S. N. Mechanical Properties of Highly Porous PDLLA/Bioglass® Composite Foams as Scaffolds for Bone Tissue Engineering. *Acta Biomaterialia* **2005**, *1* (6), 643–652. https://doi.org/10.1016/j.actbio.2005.07.003.
(28) Wang, D.; Romer, F.; Connell, L.; Walter, C.; Saiz, E.; Yue, S.; Lee, P. D.; McPhail, D. S.; Hanna, J. V.; Jones, J. R. Highly Flexible Silica/Chitosan Hybrid Scaffolds with Oriented Pores for Tissue Regeneration. *J. Mater. Chem. B* **2015**, *3* (38), 7560–7576. https://doi.org/10.1039/C5TB00767D.
(29) Martin, R. A.; Yue, S.; Hanna, J. V.; Lee, P. D.; Newport, R. J.; Smith, M. E.; Jones, J. R. Characterizing the Hierarchical Structures of Bioactive Sol-Gel Silicate Glass and Hybrid Scaffolds for Bone Regeneration. *Philosophical Transactions of the Royal Society A: Mathematical, Physical and Engineering Sciences* **2012**, *370* (1963), 1422–1443. https://doi.org/10.1098/rsta.2011.0308.
(30) Lao, J.; Dieudonné, X.; Fayon, F.; Montouillout, V.; Jallot, E. Bioactive Glass–Gelatin Hybrids: Building Scaffolds with Enhanced Calcium Incorporation and Controlled Porosity for Bone Regeneration. *J. Mater. Chem. B* **2016**, *4* (14), 2486–2497. https://doi.org/10.1039/C5TB02345A.
(31) Deville, S. *Freezing Colloids: Observations, Principles, Control, and Use: Applications in Materials Science, Life Science, Earth Science, Food Science, and Engineering*; Engineering Materials and Processes; Springer International Publishing, 2017.
(32) Shi, Q.; An, Z.; Tsung, C. K.; Liang, H.; Zheng, N.; Hawker, C. J.; Stucky, G. D. Ice-Templating of Core/Shell Microgel Fibers through "bricks-and-Mortar" Assembly. *Advanced Materials* **2007**, *19* (24), 4539–4543. https://doi.org/10.1002/adma.200700819.
(33) Boal, A. K.; Ilhan, F.; Derouchey, J. E.; Thurn-Albrecht, T.; Russell, T. P.; Rotello, V. M. Self-Assembly of Nanoparticles into Structured Spherical and Network Aggregates Multi-Scale Ordering of Materials Is Central for the Application of Molecular Systems. *Nature* **2000**, *404* (April), 746–748.
(34) Brandt, K.; Wolff, M. F. H.; Salikov, V.; Heinrich, S.; Schneider, G. A. A Novel Method for a Multi-Level Hierarchical Composite with Brick-and-Mortar Structure. *Scientific Reports* **2013**, *3*, 1–8. https://doi.org/10.1038/srep02322.
(35) Lagarrigue, P.; Soulié, J.; Grossin, D.; Dupret-Bories, A.; Combes, C.; Darcos, V. Well-Defined Polyester-Grafted Silica Nanoparticles for Biomedical Applications: Synthesis and Quantitative Characterization. *Polymer* **2020**, *211*, 123048. https://doi.org/10.1016/j.polymer.2020.123048.
(36) Greasley, S. L.; Page, S. J.; Sirovica, S.; Chen, S.; Martin, R. A.; Riveiro, A.; Hanna, J. V.; Porter, A. E.; Jones, J. R. Controlling Particle Size in the Stöber Process and Incorporation of Calcium. *Journal of Colloid and Interface Science* **2016**, *469*, 213–223. https://doi.org/10.1016/j.jcis.2016.01.065.
(37) Johnson, R. L.; Schmidt-Rohr, K. Quantitative Solid-State 13C NMR with Signal Enhancement by Multiple Cross Polarization. *Journal of Magnetic Resonance* **2014**, *239*, 44–49. https://doi.org/10.1016/j.jmr.2013.11.009.
(38) de Oliveira, A. A. R.; de Carvalho, B. B.; Sander Mansur, H.; de Magalhães Pereira, M. Synthesis and Characterization of Bioactive Glass Particles Using an Ultrasound-Assisted Sol–Gel Process: Engineering the Morphology and Size of Sonogels via a Poly(Ethylene Glycol) Dispersing Agent. *Materials Letters* **2014**, *133*, 44–48. https://doi.org/10.1016/j.matlet.2014.06.092.
(39) Guillaume, S. M.; Schappacher, M.; Soum, A. Polymerization of ε-Caprolactone Initiated by Nd(BH4)3(THF)3: Synthesis of Hydroxytelechelic Poly(ε Caprolactone). *Macromolecules* **2003**, *36* (1), 54–60. https://doi.org/10.1021/ma020993g.

(40) Hu, Y.; Darcos, V.; Monge, S.; Li, S. Synthesis and Self-Assembling of Poly(N-Isopropylacrylamide-Block-Poly(L-Lactide)-Block-Poly(N Isopropylacrylamide) Triblock Copolymers Prepared by Combination of Ring-Opening Polymerization and Atom Transfer Radical Polymerization. *J. Polym. Sci. Part A: Polym. Chem.* **2013**, *51* (15), 3274–3283. https://doi.org/10.1002/pola.26721.
(41) Vichery, C.; Nedelec, J.-M. Bioactive Glass Nanoparticles: From Synthesis to Materials Design for Biomedical Applications. *Materials* **2016**, *9* (4), 288. https://doi.org/10.3390/ma9040288.
(42) Zheng, K.; Boccaccini, A. R. Sol-Gel Processing of Bioactive Glass Nanoparticles: A Review. *Advances in Colloid and Interface Science* **2017**, *249*, 363–373. https://doi.org/10.1016/j.cis.2017.03.008.
(43) Lukowiak, A.; Lao, J.; Lacroix, J.; Nedelec, J.-M. Bioactive Glass Nanoparticles Obtained through Sol–Gel Chemistry. *Chemical Communications* **2013**, *49* (59), 6620. https://doi.org/10.1039/c3cc00003f.
(44) Tsigkou, O.; Labbaf, S.; Stevens, M. M.; Porter, A. E.; Jones, J. R. Monodispersed Bioactive Glass Submicron Particles and Their Effect on Bone Marrow and Adipose Tissue-Derived Stem Cells. *Advanced Healthcare Materials* **2014**, *3* (1), 115–125. https://doi.org/10.1002/adhm.201300126.
(45) Kesse, X.; Vichery, C.; Nedelec, J.-M. Deeper Insights into a Bioactive Glass Nanoparticle Synthesis Protocol To Control Its Morphology, Dispersibility, and Composition. *ACS Omega* **2019**, *4* (3), 5768–5775. https://doi.org/10.1021/acsomega.8b03598.
(46) Fan, J. P.; Kalia, P.; Di Silvio, L.; Huang, J. In Vitro Response of Human Osteoblasts to Multi-Step Sol–Gel Derived Bioactive Glass Nanoparticles for Bone Tissue Engineering. *Materials Science and Engineering: C* **2014**, *36*, 206–214. https://doi.org/10.1016/j.msec.2013.12.009.
(47) Xia, W.; Chang, J. Preparation and Characterization of Nano-Bioactive-Glasses (NBG) by a Quick Alkali-Mediated Sol–Gel Method. *Materials Letters* **2007**, *61* (14–15), 3251–3253. https://doi.org/10.1016/j.matlet.2006.11.048.
(48) Delben, J. R. J.; Pimentel, O. M.; Coelho, M. B.; Candelorio, P. D.; Furini, L. N.; Alencar dos Santos, F.; de Vicente, F. S.; Delben, A. A. S. T. Synthesis and Thermal Properties of Nanoparticles of Bioactive Glasses Containing Silver. *Journal of Thermal Analysis and Calorimetry* **2009**, *97* (2), 433–436. https://doi.org/10.1007/s10973-009-0086-4.
(49) El-Kady, A. M.; Ali, A. F.; Rizk, R. A.; Ahmed, M. M. Synthesis, Characterization and Microbiological Response of Silver Doped Bioactive Glass Nanoparticles. *Ceramics International* **2012**, *38* (1), 177–188. https://doi.org/10.1016/j.ceramint.2011.05.158.
(50) Ajita, J.; Saravanan, S.; Selvamurugan, N. Effect of Size of Bioactive Glass Nanoparticles on Mesenchymal Stem Cell Proliferation for Dental and Orthopedic Applications. *Materials Science and Engineering: C* **2015**, *53*, 142–149. https://doi.org/10.1016/j.msec.2015.04.041.
(51) Chevigny, C.; Dalmas, F.; Di Cola, E.; Gigmes, D.; Bertin, D.; Boué, F.; Jestin, J. Polymer-Grafted-Nanoparticles Nanocomposites: Dispersion, Grafted Chain Conformation, and Rheological Behavior. *Macromolecules* **2011**, *44* (1), 122–133. https://doi.org/10.1021/ma101332s.
(52) Chevigny, C.; Jestin, J.; Gigmes, D.; Schweins, R.; Di-Cola, E.; Dalmas, F.; Bertin, D.; Boué, F. "Wet-to-Dry" Conformational Transition of Polymer Layers Grafted to Nanoparticles in Nanocomposite. *Macromolecules* **2010**, *43* (11), 4833–4837. https://doi.org/10.1021/ma100858h.
(53) Schardosim, M.; Soulié, J.; Poquillon, D.; Cazalbou, S.; Duployer, B.; Tenailleau, C.; Rey, C.; Hübler, R.; Combes, C. Freeze-Casting for PLGA/Carbonated Apatite Composite Scaffolds: Structure and Properties. *Materials Science and Engineering: C* **2017**, *77*, 731–738. https://doi.org/10.1016/j.msec.2017.03.302.
(54) Rezwan, K.; Chen, Q. Z.; Blaker, J. J.; Boccaccini, A. R. Biodegradable and Bioactive Porous Polymer/Inorganic Composite Scaffolds for Bone Tissue Engineering. *Biomaterials* **2006**, *27* (18), 3413–3431. https://doi.org/10.1016/j.biomaterials.2006.01.039.
(55) Deville, S. Freeze-Casting of Porous Biomaterials: Structure, Properties and Opportunities. *Materials* **2010**, *3* (3), 1913–1927. https://doi.org/10.3390/ma3031913.
(56) Deville, S.; Saiz, E.; Tomsia, A. P. Ice-Templated Porous Alumina Structures. *Acta Materialia* **2007**, *55* (6), 1965–1974. https://doi.org/10.1016/j.actamat.2006.11.003.
(57) Shahbazi, M.-A.; Ghalkhani, M.; Maleki, H. Directional Freeze-Casting: A Bioinspired Method to Assemble Multifunctional Aligned Porous Structures for Advanced Applications. *Adv. Eng. Mater.* **2020**, *22* (7), 2000033. https://doi.org/10.1002/adem.202000033.
(58) Verrier, S.; Blaker, J. J.; Maquet, V.; Hench, L. L.; Boccaccini, A. R. PDLLA/Bioglass® Composites for Soft-Tissue and Hard-Tissue Engineering: An in Vitro Cell Biology Assessment. *Biomaterials* **2004**, *25* (15), 3013–3021. https://doi.org/10.1016/j.biomaterials.2003.09.081.
(59) Navarro, M.; Ginebra, M. P.; Planell, J. A.; Barrias, C. C.; Barbosa, M. A. In Vitro Degradation Behavior of a Novel Bioresorbable Composite Material Based on PLA and a Soluble CaP Glass. *Acta Biomaterialia* **2005**, *1* (4), 411–419. https://doi.org/10.1016/j.actbio.2005.03.004.

(60) Roether, J. A.; Boccaccini, A. R.; Hench, L. L.; Maquet, V.; Gautier, S.; Jérôme, R. Development and in Vitro Characterisation of Novel Bioresorbable and Bioactive Composite Materials Based on Polylactide Foams and Bioglasss for Tissue Engineering Applications. *Biomaterials* **2002**, *23*, 3871–3878.
(61) Schugens, Ch.; Maquet, V.; Grandfils, C.; Jerome, R.; Teyssie, Ph. Biodegradable and Macroporous Polylactide Implants for Cell Transplantation: 1. Preparation of Macroporous Polylactide Supports by Solid-Liquid Phase Separation. *Polymer* **1996**, *37* (6), 1027–1038. https://doi.org/10.1016/0032-3861(96)87287-9.
(62) Maquet, V.; Boccaccini, A. R.; Pravata, L.; Notingher, I.; Jérôme, R. Preparation, Characterization, and in Vitro Degradation of Bioresorbable and Bioactive Composites Based on Bioglass®-Filled Polylactide Foams. *Journal of Biomedical Materials Research Part A* **2003**, *66A* (2), 335–346. https://doi.org/10.1002/jbm.a.10587.
(63) Sun, H.; Mumby, S. J.; Maple, J. R.; Hagler, A. T. Ab Initio Calculations on Small Molecule Analogs of Polycarbonates. 10.
(64) Maquet, V.; Boccaccini, A. R.; Pravata, L.; Notingher, I.; Jérôme, R. Porous Poly(α-Hydroxyacid)/Bioglass® Composite Scaffolds for Bone Tissue Engineering. I: Preparation and in Vitro Characterisation. *Biomaterials* **2004**, *25* (18), 4185–4194. https://doi.org/10.1016/j.biomaterials.2003.10.082.
(65) Blaker, J. J.; Maquet, V.; Jérôme, R.; Boccaccini, A. R.; Nazhat, S. N. Mechanical Properties of Highly Porous PDLLA/Bioglass® Composite Foams as Scaffolds for Bone Tissue Engineering. *Acta Biomaterialia* **2005**, *1* (6), 643–652. https://doi.org/10.1016/j.actbio.2005.07.003.
(66) Giannoudis, P. V.; Dinopoulos, H.; Tsiridis, E. Bone Substitutes: An Update. *Injury* **2005**, *36* (3), S20–S27. https://doi.org/10.1016/j.injury.2005.07.029.
(67) Drouet, C.; Barré, R.; Brunel, G.; Dechambre, G.; Benqué, E.; Combes, C.; Rey, C. Impact of Calcium Phosphate Particle Morphology on Osteoconduction: An In Vivo Study. *KEM* **2007**, *361–363*, 1237–1240. https://doi.org/10.4028/www.scientific.net/KEM.361-363.1237.
(68) Scotti, K. L. Freezecasting.Net Database https://zenodo.org/record/545853 (accessed 2020 -08 -03). https://doi.org/10.5281/ZENODO.545853.
(69) Gibson, L. J.; Ashby, M. F. *Cellular Solids: Structure and Properties*, 2nd ed.; Cambridge University Press, 1997. https://doi.org/10.1017/CBO9781139878326.
(70) Arabi, N.; Zamanian, A.; Rashvand, S. N.; Ghorbani, F. The Tunable Porous Structure of Gelatin–Bioglass Nanocomposite Scaffolds for Bone Tissue Engineering Applications: Physicochemical, Mechanical, and In Vitro Properties. *Macromolecular Materials and Engineering* **2018**, *303* (3), 1700539. https://doi.org/10.1002/mame.201700539.
(71) Gibson, L. J. Biomechanics of Cellular Solids. *Journal of Biomechanics* **2005**, *38* (3), 377–399. https://doi.org/10.1016/j.jbiomech.2004.09.027.
(72) Boal, A. K.; Gray, M.; Ilhan, F.; Clavier, G. M.; Kapitzky, L.; Rotello, V. M. Bricks and Mortar Self-Assembly of Nanoparticles. *Tetrahedron* **2002**, *58* (4), 765–770. https://doi.org/10.1016/S0040-4020(01)01100-0.